# Microstructurally-guided explicit continuum models for isotropic magnetorheological elastomers with iron particles

Dipayan Mukherjee, Laurence Bodelot, Kostas Danas

# Microstructurally-guided explicit continuum models for isotropic magnetorheological elastomers with iron particles

Dipayan Mukherjee[a], Laurence Bodelot[a], Kostas Danas[a,*]

[a] *LMS, C.N.R.S, École Polytechnique, Institute Polytechnique de Paris, Palaiseau, 91128, France*

**Abstract**

This work provides a family of explicit phenomenological models both in the $\mathbf{F}-\mathbf{H}$ and $\mathbf{F}-\mathbf{B}$ variable space. These models are derived directly from an analytical implicit homogenization model for isotropic magnetorheological elastomers (MREs), which, in turn, is assessed via full-field numerical simulations. The proposed phenomenological models are constructed so that they recover the same purely mechanical, initial and saturation magnetization and initial magnetostriction response of the analytical homogenization model for all sets of material parameters, such as the particle volume fraction and the material properties of the constituents (e.g., the matrix shear modulus, the magnetic susceptibility and magnetization saturation of the particles). The functional form of the proposed phenomenological models is based on simple energy functions with small number of calibration parameters thus allowing for the description of magnetoelastic solids more generally such as anisotropic (with particle-chains) ones, polymers comprising ferrofluid particles or particle clusters. This, in turn, makes them suitable to probe a large set of experimental or numerical results. The models of the present study show that in isotropic MREs, the entire magnetization response is insensitive to the shear modulus of the matrix material even when the latter ranges between 0.003-0.3MPa, while the magnetostriction response is extremely sensitive to the mechanical properties of the matrix material.

## 1. Introduction

In recent years, there has been an increasing interest in the experimental, theoretical and numerical study of magnetoelastic and electroelastic materials that can achieve large strains under application of magnetic or electric fields, respectively. Specifically, in the context of magnetoelasticity, this has been possible by the fabrication of composite materials made of a soft matrix (such as gels, polymers and elastomers) and magnetically soft or hard but mechanically stiff particles. This class of materials has been termed magnetorheological elastomers (MREs) (Shiga et al., 1995; Jolly et al., 1996; Ginder et al., 1999; Martin et al., 2006; Diguet et al., 2010; Danas et al., 2012; Bodelot et al., 2016, 2018) or h-MREs (Schümann et al., 2017; Kim et al., 2018; Zhao et al., 2019). The MREs comprise magnetically soft iron particles with negligible magnetic hysteresis and the h-MREs consist of magnetically hard particles (such as NdFeB ones), which, in turn, lead to a strong magnetic hysteresis.

For this reason, numerous studies have been devoted to construct analytical continuum models capable of describing the magnetoelastic response of MREs materials under finite deformations and magnetic fields. These studies can be roughly classified into two categories: (*i*) top-down or phenomenological approaches in which macroscopic free energies are postulated based on macroscopic experimental observations (Kankanala and Triantafyllidis, 2004; Dorfmann and Ogden, 2005; Bustamante et al., 2011; Danas et al., 2012; Saxena et al., 2015) and (*ii*) bottom-up or homogenization approaches in which macroscopic free energies are derived based on the underlying microscopic behavior (Liu et al., 2006; Ponte Castañeda and Galipeau, 2011; Galipeau and Ponte Castañeda, 2013; Lefèvre et al., 2017). While the practical challenges of carrying out experiments that test the material (and *not* the structural) response of specimens have led to the development of numerous phenomenological models, the intrinsic mathematical challenges of carrying out the homogenization limit of the equations of magnetoelastostatics has only provided a handful of available results. Furthermore, the proposed phenomenological models have only been calibrated and assessed for the given experimental setup that have been proposed and a zoo of different expressions is now available. Yet none of these models has universal characteristics in the sense that none of these models has been used to study a wide range of materials parameters.

In parallel, numerical homogenization studies of various microstructures have been carried out in two- and three-dimensional unit cells (Javili et al., 2013; Galipeau et al., 2014; Miehe et al., 2016). In those studies, the results were obtained by using a scalar potential formulation which was presented in the context of electromechanical problems by Landis (2002) (but see also recent numerical work by Henann et al. (2013)). In more recent studies, Kästner and co-workers(Spieler et al., 2013, 2014; Metsch et al., 2016) and Danas (2017) have used the vector potential to analyze

Cite as: Int. J. Non-Linear Mech. 120 (2020) 103380, https://doi.org/10.1016/j.ijnonlinmec.2019.103380

*Corresponding author

*Email addresses:* dipayan.mukherjee@polytechnique.edu (Dipayan Mukherjee), laurence.bodelot@polytechnique.edu (Laurence Bodelot), konstantinos.danas@polytechnique.edu (Kostas Danas)

two-dimensional MREs. Moreover, in an effort to resolve some of the surrounding air and specimen effects, Kalina et al. (2016) have modeled directly the specimen, the surrounding air and the microstructure at the same scale. While this study has led to satisfactory qualitative agreement with experiments, it did not resolve the different length scales as one goes from specimen to microstructure, since that would require an untractable mesh size. Along this effort, Keip and Rambausek (2015) proposed a two-scale finite element approach in order to solve simultaneously the magneto-mechanical boundary value problem and the microstructural problem by properly resolving the separation of the very different length scales. While this last approach is the more complete one, it still remains numerically demanding, especially if complex unit cells with large number of particles are considered. Moreover, in all these approaches, it is very hard to decouple from the estimated response the relative effect of the specimen geometry and that of the microstructure.

In this regard, the recent study of Lefèvre et al. (2017) proposes an alternative view to the problem by first solving the homogenization problem at the RVE scale analytically and then using these estimates at the macroscopic scale to analyze the specimen shape effects. In that effort, the authors obtained a very useful analytical model for incompressible isotropic MREs in the space of the deformation gradient $\mathbf{F}$ and the Lagrangian $h-$field $\mathbf{H}$. This model, however, is implicit and requires the solution of a highly nonlinear algebraic equation simultaneously with the estimation of the effective energy function. In a companion paper (Lefèvre et al., 2019), the same authors proposed an approximate explicit model obtained directly by fitting the implicit variable of the original homogenization model, thus making it extremely simple for numerical implementation keeping extremely good accuracy. In turn, due to the very strong nonlinearities involved in those models, it is almost impossible to carry out an analytical partial Legendre-Fenchel transform with respect to the $\mathbf{H}$ field in order to obtain the complementary energy in terms of the deformation gradient $\mathbf{F}$ and the Lagrangian magnetic field $\mathbf{B}$. This latter $\mathbf{F}-\mathbf{B}$ version is extremely useful in numerous boundary value problems (e.g., instability problems or device-based ones where the magnetic poles and the coils are modeled directly), that are naturally written in terms of the magnetic vector potential and not the scalar potential.

Motivated by these observations, the objective of this work is to put forth a family of homogenization-guided phenomenological models for isotropic MREs in both the $\mathbf{F}-\mathbf{H}$ and $\mathbf{F}-\mathbf{B}$ space that are entirely calibrated by using the analytical implicit homogenization model of Lefèvre et al. (2017). These phenomenological models are "explicit" in both $\mathbf{F}-\mathbf{H}$ and $\mathbf{F}-\mathbf{B}$ space and thus are very simple to be implemented in any finite element user material/element code. They are constructed by a proper choice of energy functions and in such a way that recover three main features of the homogenization model: (i) they recover the exact (in the sense of homogenization) effective magnetization response at small and very large (i.e. at magnetization saturation) magnetic fields, (ii) they predict the exact magnetostriction response at small-to-moderate magnetic fields for all mechanical pre-loads and (iii) their purely mechanical response is exactly that of the homogenization model, which has been originally obtained in Lopez-Pamies et al. (2013). In addition, the proposed phenomenological models are assessed for a very large range of material responses, such as a large range of shear moduli of the matrix material and particle volume fractions. This allows to study various boundary value problems in a more predictive fashion that aids in material selection for given applications. The form of the phenomenological functions that are proposed for the coupled magneto-mechanical response is universal in the sense that they can be used to describe the magnetoelastic response of MREs from available experimental or other numerical results for anisotropic microstructures (e.g. particle-chains), or describe the response of polymer composites comprising other type of magnetoactive particles such as ferrofluids (Lefèvre et al., 2017). Also, the present phenomenological models can be used *mutatis mutandis* to describe the response of electroactive polymers with (Lefèvre and Lopez-Pamies, 2016a,b) or without dielectric particles (Zurlo et al., 2018). Finally, an ad-hoc extension of these models in the context of *nearly* incompressible MREs is proposed allowing for an even more simplified implementation in numerical codes.

The presentation of the work is organized as follows. Section 2 discusses basic definitions in the context of coupled magneto-elasticity. In Section 3, we formulate the homogenization problem in the $\mathbf{F}-\mathbf{H}$ space, we recall the definitions of the effective energy and propose, following the recent work of Danas (2017), an augmented variational framework that allows for the proper definition of an RVE and the corresponding effective magnetization and magnetostriction free from specimen shape effects. We then devote Section 4 to the presentation of the analytical homogenization and phenomenological models in the $\mathbf{F}-\mathbf{H}$ and $\mathbf{F}-\mathbf{B}$ space. Therein, we discuss in detail the construction of the phenomenological models and the calibration of their coefficients by proper expansions at small mechanical and magnetic fields. This section finishes with the discussion of the numerical finite element RVE problem. The assessment of all the models is done in Section 5, where we study a wide range of material parameters, while we also explore the response of the phenomenological models beyond the regime of calibration by analyzing the effect of mechanical pre-stress upon the magnetization and magnetostriction response of the MRE. Finally, in Section 6, we record some concluding remarks.

## 2. Preliminary definitions

We consider a deformable solid occupying a volume $\mathcal{V}_0 \in \mathbb{R}^3$ with boundary $\partial\mathcal{V}_0 \in \mathbb{R}^2$ in its reference configuration. The deformation of the solid from its reference configuration $\mathcal{V}_0$ to the current configuration $\mathcal{V}$ is defined in terms of a continuous and one-to-one mapping $\mathbf{y}(\mathbf{X})$. We assume $\mathbf{y}$ to be continuous and twice differentiable in $\mathcal{V}_0$, except at the material interfaces. Thus, the position vector of a material point in the current configuration is given by $\mathbf{x} = \mathbf{y}(\mathbf{X})$. The deformation gradient is therefore defined as $\breve{\mathbf{F}}(\mathbf{X}) = \operatorname{Grad}\mathbf{y}$[1] with $\breve{J} = \det\breve{\mathbf{F}} > 0$, where Grad denotes the gradient

[1]Henceforth, the notation $\breve{(\cdot)}$ is used to denote local microscopic quantities, whereas plain symbols refer to the macroscopic scale.

operator with respect to $\mathbf{X}$. We consider no time dependence.

The purely magnetic problem may be described in terms of the Eulerian magnetic field $\breve{\mathbf{b}}$, whose work conjugate is referred to as the magnetic $h$-field $\breve{\mathbf{h}}$. The current magnetization $\breve{\mathbf{m}}$ is then defined by the constitutive relation

$$\breve{\mathbf{b}} = \mu_0(\breve{\mathbf{h}} + \breve{\mathbf{m}}), \tag{1}$$

where $\mu_0$ is the magnetic permeability of free space to be defined later. In case of a non-magnetic medium, e.g., air, the magnetization $\breve{\mathbf{m}}$ vanishes reducing (1) to $\breve{\mathbf{b}} = \mu_0\breve{\mathbf{h}}$. In principle, the magnetic problem can be expressed in terms of $\breve{\mathbf{b}}$, $\breve{\mathbf{h}}$ or $\breve{\mathbf{m}}$ as the independent variable, see for instance (Kankanala and Triantafyllidis, 2004). In fact, in a coupled magneto-mechanical problem, one can retrieve the $\breve{\mathbf{h}}$-based formulation from the $\breve{\mathbf{b}}$ form by performing a partial Legendre-Frechel transform of the total energy functional with respect to $\breve{\mathbf{b}}$ and vice-versa (Danas, 2017). Both $\breve{\mathbf{b}}$ and $\breve{\mathbf{h}}$ are Eulerian quantities and are subjected to well-defined differential and boundary constrains arising directly from the magnetic balance laws. The magnetization $\breve{\mathbf{m}}$ is also an Eulerian quantity on which, in turn, no differential and/or boundary constraints are imposed.

The Lagrangian counterparts of the divergence-free $\breve{\mathbf{b}}$ and the curl-free $\breve{\mathbf{h}}$ are obtained by a pull-back operation on the global balance equations (Dorfmann and Ogden, 2004), such that

$$\breve{\mathbf{B}} = \breve{J}\breve{\mathbf{F}}^{-1}\breve{\mathbf{b}} \qquad \text{and} \qquad \breve{\mathbf{H}} = \breve{\mathbf{F}}^{T}\breve{\mathbf{h}}, \tag{2}$$

respectively. Given the Lagrangian $\breve{\mathbf{B}}$ and $\breve{\mathbf{H}}$ as in (2), it is evident that (1) is non-unique under pull-back transformations, also implying the non-uniqueness of the Lagrangian form of $\breve{\mathbf{m}}$ (Dorfmann and Ogden, 2004, 2005; Kankanala and Triantafyllidis, 2004). Therefore, no attempt is made to provide a Lagrangian form of $\breve{\mathbf{m}}$. The Lagrangian $\breve{\mathbf{B}}$ and $\breve{\mathbf{H}}$ fields also satisfy the divergence and curl free conditions, respectively, so that (Kankanala and Triantafyllidis, 2004; Dorfmann and Ogden, 2005)

$$\mathrm{Div}\,\breve{\mathbf{B}} = 0 \quad \text{in} \quad \mathcal{V}_0 \qquad \text{with} \qquad \boldsymbol{\mathcal{N}} \cdot \left[\!\left[\breve{\mathbf{B}}\right]\!\right] = 0 \quad \text{on} \quad \partial\mathcal{V}_0, \tag{3}$$

$$\mathrm{Curl}\,\breve{\mathbf{H}} = 0 \quad \text{in} \quad \mathcal{V}_0 \qquad \text{with} \qquad \boldsymbol{\mathcal{N}} \times \left[\!\left[\breve{\mathbf{H}}\right]\!\right] = 0 \quad \text{on} \quad \partial\mathcal{V}_0, \tag{4}$$

where $[\![\cdot]\!]$ denotes the jump across the boundary $\partial\mathcal{V}_0$ whose normal is denoted with $\boldsymbol{\mathcal{N}}$. The former allows us to express $\breve{\mathbf{B}}$ as the curl of a vector potential $\mathcal{A}$, i.e., $\breve{\mathbf{B}} = \mathrm{Curl}\mathcal{A}$, whereas the latter leads to an expression of $\breve{\mathbf{H}}$ in terms of the gradient of a scalar potential, such that, $\breve{\mathbf{H}} = -\mathrm{Grad}\varphi$. Such vector/scalar potential-based formulations are used extensively in the numerical realization of coupled magneto-mechanical boundary value problems (Lefèvre et al., 2017; Danas, 2017; Psarra et al., 2017). In fact, from a purely computational point of view, the scalar potential-based formulation is simpler to implement due to the use of a single additional scalar degree of freedom, i.e., the scalar potential. For the purposes of the present work, this is sufficient since we are interested in the constitutive response of MREs. The reader is referred to (Danas, 2017) for an equivalent vector potential-based formulation.

An equivalent set of the magnetostatic balance laws in terms of the Eulerian $\breve{\mathbf{b}}$ and $\breve{\mathbf{h}}$ fields can be obtained by substituting (2) into (3) and (4). The resulting counterparts of (3) and (4) that hold in the current configuration are then given by (Kankanala and Triantafyllidis, 2004; Dorfmann and Ogden, 2005)

$$\mathrm{div}\,\breve{\mathbf{b}} = 0 \quad \text{in} \quad \mathcal{V} \qquad \text{with} \qquad \mathbf{n} \cdot \left[\!\left[\breve{\mathbf{b}}\right]\!\right] = 0 \quad \text{on} \quad \partial\mathcal{V}, \tag{5}$$

$$\mathrm{curl}\,\breve{\mathbf{h}} = 0 \quad \text{in} \quad \mathcal{V} \qquad \text{with} \qquad \mathbf{n} \times \left[\!\left[\breve{\mathbf{h}}\right]\!\right] = 0 \quad \text{on} \quad \partial\mathcal{V}, \tag{6}$$

where "div" and "curl" represent, respectively, the divergence and curl operations in the current configuration and $\mathbf{n}$ is the unit normal on the current boundary $\partial\mathcal{V}$.

Finally, the energy per unit volume of an isotropic, magneto-hyperelastic solid in its reference configuration may be given in terms of the deformation gradient $\breve{\mathbf{F}}$ and the Lagrangian $h-$field $\breve{\mathbf{H}}$ by

$$W(\mathbf{X}, \breve{\mathbf{F}}, \breve{\mathbf{H}}) = \Phi(\mathbf{X}, \breve{\mathbf{F}}, \breve{\mathbf{H}}) - \frac{\mu_0}{2}\breve{J}\breve{\mathbf{F}}^{-T}\breve{\mathbf{H}} \cdot \breve{\mathbf{F}}^{-T}\breve{\mathbf{H}}. \tag{7}$$

In this expression, $\Phi(\mathbf{X}, \breve{\mathbf{F}}, \breve{\mathbf{H}})$ is the specific free energy of the system, while the second term is used to describe the magnetic energy of the surroundings (ether) and is present always irrespective of whether the medium is magnetic or not (Dorfmann and Ogden, 2005; Danas, 2017). No effect of magnetic/elastic dissipation is considered. Furthermore, in the above description, we use $\breve{\mathbf{H}}$ as an independent variable. An equivalent description and analysis using $\breve{\mathbf{B}}$ as an independent variable has been discussed extensively in Danas (2017) for the homogenization problem and is not repeated here.

Hence, by standard thermodynamic arguments, one can obtain the constitutive relations (Kankanala and Triantafyllidis, 2004; Dorfmann and Ogden, 2005; Bustamante et al., 2008; Lefèvre et al., 2017)

$$\breve{\mathbf{S}} = \frac{\partial W}{\partial \breve{\mathbf{F}}}(\mathbf{X}, \breve{\mathbf{F}}, \breve{\mathbf{H}}) \qquad \text{and} \qquad \breve{\mathbf{B}} = -\frac{\partial W}{\partial \breve{\mathbf{H}}}(\mathbf{X}, \breve{\mathbf{F}}, \breve{\mathbf{H}}) \tag{8}$$

for the local first Piola-Kirchhoff stress and the local magnetic field, respectively. Several phenomenological energy functions have been proposed for both isotropic (Bustamante, 2010) and transversely isotropic (Danas et al., 2012) MREs. In the following sections, we first consider fully decoupled energy functions for each constituent, i.e., the polymer matrix phase and the particle magnetic phase to obtain an effective macroscopic response of the composite via analytical and numerical homogenization.

Finally, it is worth noting that the local Piola-Kirchhoff and Cauchy stresses may be written as a sum of the local mechanical and Maxwell stresses (Kankanala and Triantafyllidis, 2004; Dorfmann and Ogden, 2005; Bustamante et al., 2008). For the case of an energy function that depends on $\breve{\mathbf{F}}$ and $\breve{\mathbf{H}}$, one can show that (Kankanala and Triantafyllidis, 2004)

$$\breve{\mathbf{S}} = \breve{J}\breve{\boldsymbol{\sigma}}\breve{\mathbf{F}}^{-T}, \quad \breve{\boldsymbol{\sigma}} = \breve{\boldsymbol{\sigma}}_{\mathtt{mech}} + \breve{\boldsymbol{\sigma}}_{\mathtt{maxw}}, \qquad \text{with} \qquad \breve{\boldsymbol{\sigma}}_{\mathtt{maxw}} = \breve{\mathbf{h}}\,\breve{\mathbf{b}} - \frac{\mu_0}{2}|\breve{\mathbf{h}}|^2\mathbf{I}, \tag{9}$$

where $|\cdot|$ represents the standard Euclidean norm and $\mathbf{I}$ is the second order identity tensor. In the absence of mechanical body forces, the stress measures, $\breve{\mathbf{S}}$ and $\breve{\boldsymbol{\sigma}}$[2], are divergence-free leading to the balance laws

$$\operatorname{Div}\breve{\mathbf{S}} = 0 \quad \text{in} \quad \mathcal{V}_0 \qquad \text{with} \qquad \boldsymbol{\mathcal{N}}\cdot\left[\!\left[\breve{\mathbf{S}}\right]\!\right] = \breve{\mathbf{T}} \quad \text{on} \quad \partial\mathcal{V}_0, \tag{10}$$

$$\operatorname{div}\breve{\boldsymbol{\sigma}} = 0 \quad \text{in} \quad \mathcal{V} \qquad \text{with} \qquad \mathbf{n}\cdot[\![\breve{\boldsymbol{\sigma}}]\!] = \breve{\mathbf{t}} \quad \text{on} \quad \partial\mathcal{V}, \tag{11}$$

in the reference and current configuration, respectively. The Lagrangian (Eulerian) boundary traction on $\partial\mathcal{V}_0$ ($\partial\mathcal{V}$) is denoted by $\breve{\mathbf{T}}$ ($\breve{\mathbf{t}}$) in (10) ((11)).

## 3. Micro-magneto-mechanical modeling of MREs

This section describes the general steps towards the numerical and theoretical modeling of particle-filled MREs. We first define the constitutive models for the individual phases of the composite. This is followed by laying out the periodic homogenization framework in order to obtain the effective (macroscopic) response of the composite. It should be noted that the following expressions are presented in the general compressible case, while both the incompressible and compressible cases are studied in the following sections. Whenever necessary, special care is taken to clarify the differences between these two descriptions.

### *3.1. Local constitutive models for the constituents*

We consider a composite material consisting of a matrix phase, denoted with $\mathtt{i} = \mathtt{m}$ and a particle phase, denoted with $\mathtt{i} = \mathtt{p}$. For the sake of presentation, we assume both phases to be magnetoelastic, whereas the special case of a polymeric non-magnetic matrix or rigid mechanically particle can be easily obtained later. Each phase occupies a sub-domain $\mathcal{V}_0^{\mathtt{m}}$ and $\mathcal{V}_0^{\mathtt{p}}$, respectively, in the reference configuration. The local energy associated with such a composite is then given by

$$W(\mathbf{X}, \breve{\mathbf{F}}, \breve{\mathbf{H}}) = \Theta(\mathbf{X})W_{\mathtt{m}}(\breve{\mathbf{F}}, \breve{\mathbf{H}}) + (1 - \Theta(\mathbf{X}))W_{\mathtt{p}}(\breve{\mathbf{F}}, \breve{\mathbf{H}}),$$

where the function $\Theta(\mathbf{X})$ is the characteristic function and takes the value $\Theta(\mathbf{X}) = 1$ if $\mathbf{X} \in \mathcal{V}_0^{\mathtt{m}}$ and $\Theta(\mathbf{X}) = 0$ if $\mathbf{X} \in \mathcal{V}_0^{\mathtt{p}}$. These characteristic functions must comply with the hypothesis of the separation of length scales, i.e., $\Theta$ must vary in a length scale that is much smaller than the length scale of the representative volume element (RVE) under study. The energy associated with an individual phase is then given by $W_{\mathtt{i}}(\breve{\mathbf{F}}, \breve{\mathbf{H}}) \equiv w_{\mathtt{i}}(\breve{\mathbf{F}}, \breve{\mathbf{h}})$ with $\mathtt{i} = \mathtt{m}$ or $\mathtt{i} = \mathtt{p}$, and reads

$$W_{\mathtt{i}}(\breve{\mathbf{F}}, \breve{\mathbf{H}}) = \Phi_{\mathtt{i}}(\breve{\mathbf{F}}, \breve{\mathbf{H}}) - \frac{\mu_0}{2}\breve{J}\breve{\mathbf{F}}^{-T}\breve{\mathbf{H}}\cdot\breve{\mathbf{F}}^{-T}\breve{\mathbf{H}} = \phi_{\mathtt{i}}(\breve{\mathbf{F}}, \breve{\mathbf{h}}) - \frac{\mu_0}{2}\breve{J}\breve{\mathbf{h}}\cdot\breve{\mathbf{h}} = w_{\mathtt{i}}(\breve{\mathbf{F}}, \breve{\mathbf{h}}). \tag{12}$$

Here, we used the transformation relation $(2)_2$ to obtain the equivalent energy $w_{\mathtt{i}}(\breve{\mathbf{F}}, \breve{\mathbf{h}})$ in terms of the Eulerian $h$-field $\breve{\mathbf{h}}$. The specific free energy $\Phi_{\mathtt{i}}(\breve{\mathbf{F}}, \breve{\mathbf{H}})$ is typically decomposed into a purely mechanical and a magneto-mechanical part (Danas et al., 2012; Javili et al., 2013; Lefèvre et al., 2017; Danas, 2017)

$$\Phi_{\mathtt{i}}(\breve{\mathbf{F}}, \breve{\mathbf{H}}) = \Phi_{\mathtt{i}}^{\mathtt{mech}}(\breve{\mathbf{F}}) + \Phi_{\mathtt{i}}^{\mathtt{mag}}(\breve{\mathbf{F}}, \breve{\mathbf{H}}), \tag{13}$$

where the subscript "*mech*" denotes the purely mechanical part and the subscript "*mag*" represents the magneto-mechanical part of the total $\Phi_{\mathtt{i}}(\breve{\mathbf{F}}, \breve{\mathbf{H}})$. Such a decomposition is fairly general but is more than sufficient for phases that are not magnetic or exhibit a very minor magneto-mechanical coupling, such as the iron particles which are very stiff mechanically and thus attain very small magnetostrictive strains (e.g. in the order of $10^{-6} - 10^{-5}$). Furthermore, material objectivity is readily satisfied by expressing $\Phi_{\mathtt{i}}(\breve{\mathbf{F}}, \breve{\mathbf{H}})$ in terms of six invariants as listed in Table 1.

[2]Note that the expression for the Maxwell stress depends on the choice of the independent magnetic variables as discussed in Kankanala and Triantafyllidis (2004).

Table 1: Invariants associated with isotropic magneto-elastic solids

| Mechanical | | Magneto-mechanical | | |
|---|---|---|---|---|
| Invariant | Expression | Invariant | Lagrangian | Eulerian |
| $\breve{I}_1 =$ | $\mathrm{tr}(\breve{\mathbf{F}}^T\breve{\mathbf{F}})$ | $\breve{I}_4^H =$ | $\breve{\mathbf{H}}\cdot\breve{\mathbf{H}}$ | $\breve{\mathbf{F}}^T\breve{\mathbf{h}}\cdot\breve{\mathbf{F}}^T\breve{\mathbf{h}}$ |
| $\breve{I}_2 =$ | $\frac{1}{2}[\{\mathrm{tr}(\breve{\mathbf{F}}^T\breve{\mathbf{F}})\}^2 - \breve{\mathbf{F}}^T\breve{\mathbf{F}}\cdot\breve{\mathbf{F}}^T\breve{\mathbf{F}}]$ | $\breve{I}_5^H =$ | $\breve{\mathbf{F}}^{-T}\breve{\mathbf{H}}\cdot\breve{\mathbf{F}}^{-T}\breve{\mathbf{H}}$ | $\breve{\mathbf{h}}\cdot\breve{\mathbf{h}}$ |
| $\breve{I}_3 = \breve{J} =$ | $\det\breve{\mathbf{F}}$ | $\breve{I}_6^H =$ | $\breve{\mathbf{F}}^{-1}\breve{\mathbf{F}}^{-T}\breve{\mathbf{H}}\cdot\breve{\mathbf{F}}^{-1}\breve{\mathbf{F}}^{-T}\breve{\mathbf{H}}$ | $\breve{\mathbf{F}}^{-1}\breve{\mathbf{h}}\cdot\breve{\mathbf{F}}^{-1}\breve{\mathbf{h}}$ |

In this table, the first three invariants are purely mechanical. In turn, invariants $\breve{I}_4 - \breve{I}_6$ should be discussed with caution. Following the discussion in Danas (2017), if one applies the Eulerian magnetic field $\breve{\mathbf{h}}$, then $\breve{I}_5$ is a purely magnetic invariant leading to no coupling. Instead, if one applies the Lagrangian $\breve{\mathbf{H}}$ field[3], the uncoupled magnetic invariant is $\breve{I}_4$. This subtle point is a source of discrepancies in the literature of magneto-elastic and electro-active solids and caution should be taken when one proposes constitutive laws. This distinction will be discussed in more detail in the subsequent sections when selecting the invariants for the coupled magneto-mechanical response.

Very often, the mechanical response of the magneto-elastic solids is described by a simple Neo-Hookean model, such as

$$\Phi_{\mathtt{i}}^{\mathtt{mech}}(\breve{\mathbf{F}}) = \frac{G_{\mathtt{i}}}{2}(\breve{I}_1 - 3 - 2\ln\breve{J}) + \frac{G'_{\mathtt{i}}}{2}(\breve{J}-1)^2, \quad \mathtt{i} = \mathtt{m},\,\mathtt{p}. \tag{14}$$

In this expression, $G_{\mathtt{i}}$ is the shear modulus and $G'_{\mathtt{i}}$ is the Lame constant associated with the compressibility of each phase $\mathtt{i} = \mathtt{m}, \mathtt{p}$. In the subsequent proposed homogenization and phenomenological models the use of Neo-Hookean model is not at all a prerequisite. Instead, the mechanical part of the proposed models in the present study is directly based on the work of Lopez-Pamies et al. (2013) and are valid for any matrix that is described by a $I_1-$based mechanical energy density.

For the magnetic part, a Langevin-type saturation function is used in the present study (Lefèvre et al., 2017)

$$\begin{aligned}\Phi_{\mathtt{i}}^{\mathtt{mag}}(\breve{\mathbf{F}},\breve{\mathbf{H}}) &= -\frac{\breve{J}\mu_0(m_{\mathtt{i}}^s)^2}{3\chi_{\mathtt{i}}}\left\{\ln\left[\sinh\left(\frac{3\chi_{\mathtt{i}}}{m_{\mathtt{i}}^s}\sqrt{\breve{I}_5^H}\right)\right] - \ln\left[\frac{3\chi_{\mathtt{i}}}{m_{\mathtt{i}}^s}\sqrt{\breve{I}_5^H}\right]\right\}\\ &= -\frac{\breve{J}\mu_0(m_{\mathtt{i}}^s)^2}{3\chi_{\mathtt{i}}}\left\{\ln\left[\sinh\left(\frac{3\chi_{\mathtt{i}}}{m_{\mathtt{i}}^s}|\breve{\mathbf{h}}|\right)\right] - \ln\left[\frac{3\chi_{\mathtt{i}}}{m_{\mathtt{i}}^s}|\breve{\mathbf{h}}|\right]\right\} = \phi_{\mathtt{i}}^{\mathtt{mag}}(\breve{J},\breve{\mathbf{h}}).\end{aligned} \tag{15}$$

Here, $\breve{I}_5^H$ is defined in Table 1, whereas $\chi_{\mathtt{i}}$ and $m_{\mathtt{i}}^s$ are the magnetic susceptibility and the saturation magnetization of each phase $\mathtt{i} = \mathtt{m}, \mathtt{p}$. Again, the proposed models in the following section can deal with any type of saturation functions such as the hyperbolic tangent (see Danas (2017)). We further note that as a consequence of the definition of $\breve{I}_5^H$, $\phi_{\mathtt{i}}^{\mathtt{mag}}$ depends on $\breve{\mathbf{F}}$ only via $\breve{J}$ if the Eulerian field $\breve{\mathbf{h}}$ is prescribed. Even more, in the incompressible limit, where $\breve{J}=1$, the $\phi_{\mathtt{i}}^{\mathtt{mag}}$ depends only on $\breve{\mathbf{h}}$ thus leading to no magneto-mechanical coupling in this last case. The situation is of course different if the Lagrangian field $\breve{\mathbf{H}}$ is prescribed. This point has been raised recently by Danas (2017) in order to distinguish the case of MREs and electroactive polymers.

Using next the energy (15) and the Langevin function

$$\mathcal{L}(x) = \coth x - x^{-1}, \qquad x\in\mathbb{R}, \tag{16}$$

one obtains by applying relation $(8)_2$

$$\breve{\mathbf{B}}(\breve{\mathbf{F}},\breve{\mathbf{H}}) = -\frac{\partial W_{\mathtt{i}}}{\partial\breve{\mathbf{H}}} = \mu_0\breve{J}\left[1 + \frac{m_{\mathtt{i}}^s}{\sqrt{\breve{I}_5^H}}\mathcal{L}\left(\frac{3\chi_{\mathtt{i}}\sqrt{\breve{I}_5^H}}{m_{\mathtt{i}}^s}\right)\right]\breve{\mathbf{F}}^{-1}\cdot\breve{\mathbf{F}}^{-T}\breve{\mathbf{H}}, \tag{17}$$

which becomes by use of relation (2)

$$\breve{\mathbf{b}}(\breve{\mathbf{h}}) = \mu_0\left[\breve{\mathbf{h}} + m_{\mathtt{i}}^s\mathcal{L}\left(\frac{3\chi_{\mathtt{i}}|\breve{\mathbf{h}}|}{m_{\mathtt{i}}^s}\right)\frac{\breve{\mathbf{h}}}{|\breve{\mathbf{h}}|}\right]. \tag{18}$$

The magnetization is then simply given by matching definition (1) with the last equation (18), such that

$$\breve{\mathbf{m}}(\breve{\mathbf{h}}) = m_{\mathtt{i}}^s\mathcal{L}\left(\frac{3\chi_{\mathtt{i}}|\breve{\mathbf{h}}|}{m_{\mathtt{i}}^s}\right)\frac{\breve{\mathbf{h}}}{|\breve{\mathbf{h}}|}. \tag{19}$$

In the limit of $|\breve{\mathbf{H}}|\to 0$, definition (15) becomes quadratic in $\breve{\mathbf{H}}$ (or $\breve{\mathbf{h}}$), such that

$$\Phi_{\mathtt{i}}^{\mathtt{mag}}(\breve{\mathbf{F}},\breve{\mathbf{H}}) = -\frac{\breve{J}\mu_0\chi_{\mathtt{i}}}{2}I_5^H = -\frac{\mu_0\chi_{\mathtt{i}}}{2}\breve{J}\breve{\mathbf{h}}\cdot\breve{\mathbf{h}} = \phi_{\mathtt{i}}^{\mathtt{mag}}(\breve{J},\breve{\mathbf{h}}), \quad \mathtt{i} = \mathtt{m},\,\mathtt{p}. \tag{20}$$

[3]This is the case in the context of electro-active problems where electrodes are directly attached on the boundary of the specimen and thus the electric field follows the deformation of the solid and is Lagrangian in nature.

By applying again $(8)_2$ and (2), the last relation (20) leads readily to a linear magnetic response, which can be written in terms of the magnetic permeability of phase $r$ as

$$\breve{\mathbf{b}} = \mu_{\mathtt{i}} \breve{\mathbf{h}}, \qquad \mu_{\mathtt{i}} = (1 + \chi_{\mathtt{i}})\ \mu_0, \quad \mathtt{i} = \mathtt{m}, \mathtt{p}. \tag{21}$$

*3.2. Periodic homogenization framework*

In this section, we describe briefly the periodic homogenization framework in the context of a magnetoelastic composite. Specifically, the typical size of the iron particle-filled MRE samples, that are used in the experiments, ranges from $2 - 100$ mm, whereas the average size of the iron particles is in the order $\sim 5$ $\mu$m (Danas et al., 2012; Semisalova et al., 2013; Bodelot et al., 2018). This implies that the local interactions between the magnetized iron particles take place at a scale that is substantially smaller than the specimen itself and the variation of the loading conditions. Hence, the assumption of the separation of length scales, which is necessary for the homogenization theory, turns out to be valid for such materials to a large extent (at least up to the point where macroscopic instabilities occur). Moreover, a slow variation of the microstructure of the MRE sample is further assumed, allowing to define a representative material volume $\mathcal{V}_0^{\#} \in \mathcal{V}_0$. The smallest volume $\mathcal{V}_0^{\#}$ that describes on average the response of the MRE is the representative volume element (RVE). A more complete discussion of the various scales and assumption is presented in Danas (2017) and is omitted in the present work for brevity and conciseness.

Given the aforementioned assumptions for $\mathcal{V}_0^{\#}$, the average $\mathbf{F}$ and $\mathbf{H}$ are then obtained from the local $\breve{\mathbf{F}}$ and $\breve{\mathbf{H}}$ of $\mathcal{V}_0^{\#}$ in terms of their volume average

$$\mathbf{F} = \frac{1}{\mathcal{V}_0^{\#}} \int_{\mathcal{V}_0^{\#}} \breve{\mathbf{F}}(\mathbf{X}) \mathrm{d}V \qquad \text{and} \qquad \mathbf{H} = \frac{1}{\mathcal{V}_0^{\#}} \int_{\mathcal{V}_0^{\#}} \breve{\mathbf{H}}(\mathbf{X}) \mathrm{d}V, \tag{22}$$

respectively. The periodicity condition in $\mathcal{V}_0^{\#}$ leads to a representation of the local displacement $\breve{\mathbf{u}}(\mathbf{X})$ and the scalar potential $\breve{\varphi}(\mathbf{X})$ fields in terms of their zero-average periodic fields $\widetilde{\mathbf{u}}(\mathbf{X})$ and $\widetilde{\varphi}(\mathbf{X})$ as well as the average fields $\mathbf{u} = (\mathbf{F}-\mathbf{I})\cdot\mathbf{X}$ and $\varphi = -\mathbf{H}\cdot\mathbf{X}$, respectively, such that

$$\breve{\mathbf{u}}(\mathbf{X}) = (\mathbf{F} - \mathbf{I}) \cdot \mathbf{X} + \widetilde{\mathbf{u}}(\mathbf{X}) \quad \text{and} \quad \breve{\varphi}(\mathbf{X}) = -\mathbf{H} \cdot \mathbf{X} + \widetilde{\varphi}(\mathbf{X}), \quad \forall \mathbf{X} \in \mathcal{V}_0^{\#}. \tag{23}$$

Equation (22) may be directly obtained by (23) and use of the zero average of the perturbation fields $\widetilde{\mathbf{u}}$ and $\widetilde{\varphi}$. Moreover, use of the push-forward transformation $(2)_2$ for $\breve{\mathbf{H}}$ together with the Hill-Mandel lemma and $(23)_2$ one obtains (see Appendix A for details)

$$\mathbf{h} = \frac{1}{\mathcal{V}^{\#}} \int_{\mathcal{V}^{\#}} \breve{\mathbf{h}}(\mathbf{x}) \mathrm{d}v = \mathbf{F}^{-T}\mathbf{H}. \tag{24}$$

Furthermore, the periodicity conditions (23) also imply that the magnetic fields can be decomposed into an average magnetic field $\mathbf{h}$ and a perturbation magnetic field (with zero average) $\widetilde{\mathbf{h}}$, such that the true magnetic field $\breve{\mathbf{h}}$ becomes

$$\breve{\mathbf{h}} = \mathbf{h} + \widetilde{\mathbf{h}}, \quad \text{or} \quad \breve{\mathbf{H}} = \mathbf{H} + \widetilde{\mathbf{H}}, \tag{25}$$

with $\widetilde{\mathbf{H}} = -\mathrm{Grad}\widetilde{\varphi}$.

The Hill-Mandel lemma and the periodicity conditions (23) allow to state the homogenization problem as the following optimization problem (Ponte Castañeda and Galipeau, 2011; Lopez-Pamies, 2014; Lefèvre et al., 2017)

$$W^H(\mathbf{F}, \mathbf{H}) = \inf_{\breve{\mathbf{u}} \in \mathcal{K}(\mathbf{F})} \sup_{\breve{\varphi} \in \mathcal{G}(\mathbf{H})} \frac{1}{\mathcal{V}_0^{\#}} \int_{\mathcal{V}_0^{\#}} W(\mathbf{X}, \breve{\mathbf{F}}, \breve{\mathbf{H}}) \mathrm{d}V. \tag{26}$$

Here, $\mathcal{K}$ and $\mathcal{G}$ denotes the admissible sets for $\breve{\mathbf{u}}$ and $\breve{\varphi}$ given by

$$\mathcal{K}(\mathbf{F}) = \left\{ \breve{\mathbf{F}} : \exists\ \mathbf{x} = \mathbf{y}(\mathbf{X}) \text{ with } \breve{\mathbf{F}} = \mathbf{I} + \mathrm{Grad}\breve{\mathbf{u}},\ \breve{J} > 0,\ \breve{\mathbf{u}} = (\mathbf{F} - \mathbf{I})\mathbf{X} + \widetilde{\mathbf{u}},\ \widetilde{\mathbf{u}} \text{ periodic in } \mathcal{V}_0^{\#} \right\} \tag{27}$$

and

$$\mathcal{G}(\mathbf{H}) = \left\{ \breve{\mathbf{H}} : \exists\ \mathbf{x} = \mathbf{y}(\mathbf{X}) \text{ with } \breve{\mathbf{H}} = -\mathrm{Grad}\breve{\varphi},\ \breve{\varphi} = -\mathbf{H} \cdot \mathbf{X} + \widetilde{\varphi},\ \widetilde{\varphi} \text{ periodic in } \mathcal{V}_0^{\#} \right\}, \tag{28}$$

respectively.

It can be shown (Ponte Castañeda and Galipeau, 2011; Javili et al., 2013; Lopez-Pamies, 2014; Lefèvre et al., 2017) that the effective (macroscopic) stress $\mathbf{S}$ and magnetic field $\mathbf{B}$ satisfy the homogenized constitutive relations

$$\mathbf{S} = \frac{\partial W^H}{\partial \mathbf{F}}(\mathbf{F}, \mathbf{H}) = J\boldsymbol{\sigma}\mathbf{F}^{-T}, \qquad \mathbf{B} = -\frac{\partial W^H}{\partial \mathbf{H}}(\mathbf{F}, \mathbf{H}) = \frac{1}{J}\mathbf{F}^{-1}\mathbf{b}, \tag{29}$$

where $\boldsymbol{\sigma}$ is the effective Cauchy stress, $\mathbf{b}$ is the effective Eulerian magnetic field and $J = \det \mathbf{F}$. Note that the effective first Piola-Kirchhoff stress $\mathbf{S}$ and the effective Cauchy stress $\boldsymbol{\sigma}$ are total stresses containing both mechanical and Maxwell stresses.

The developed magnetoelastic homogenization framework (26) is so far identical to the electro-active homogenization problem (Lopez-Pamies, 2014; Lefèvre and Lopez-Pamies, 2016a,b). However, the boundary conditions, to which a magneto-active elastomer is subjected to, is usually very different from the electro-active experiments. A MRE is typically placed far from the fixed magnetic poles, which essentially creates a Eulerian background magnetic field in between them (Psarra et al., 2017; Bodelot et al., 2018). On the other hand, electrodes are typically sprayed on an electro-active soft composite to apply an electric field directly on the boundary of the composite. This fundamental difference between the magneto- and electro-active problems necessitates a correction to (26), which is, in its present form, the complete variational problem for electro-active composites (Danas, 2017).

We note that in a magnetoelastic RVE, the mechanical stress, $\mathbf{S}_{\texttt{mech}}$, is a direct consequence of the rearrangement of the iron particles, which move due to the applied background Eulerian magnetic field as well as due to inter-particle interactions. In turn, the average Maxwell stress, $\mathbf{S}_{\texttt{maxw}}$, is present in an RVE and its neighboring RVEs because of the average magnetostatic energy. Owing to the fact that in a slowly changing microstructure, the neighboring RVEs have the same average magnetization $\mathbf{m}$ and thus average magnetostatic energy, we can completely disregard the effect of $\mathbf{S}_{\texttt{maxw}}$ in the mechanical deformation of a magentoelastic RVE (see Danas (2017) for more details).

But first, one needs to identify $\mathbf{S}_{\texttt{maxw}}$ from (26). For this, we recast $W^H(\mathbf{F},\mathbf{H})$ explicitly in terms of the effective free energy $\Phi^H(\mathbf{F},\mathbf{H})$ and the energy contribution due to the background magnetic field, such that

$$W^H(\mathbf{F},\mathbf{H}) = \Phi^H(\mathbf{F},\mathbf{H}) - \frac{\mu_0}{2} J\mathbf{F}^{-T}\mathbf{H}\cdot\mathbf{F}^{-T}\mathbf{H} = \phi^h(\mathbf{F},\mathbf{h}) - \frac{\mu_0}{2} J\mathbf{h}\cdot\mathbf{h} = w^h(\mathbf{F},\mathbf{h}). \tag{30}$$

The total effective stress $\mathbf{S}$ can then be obtained via $(29)_1$. However, as it was shown in Danas (2017), it is difficult to identify the complete Lagrangian average Maxwell stress given a prescribed Eulerian field $\breve{\mathbf{h}}$. Instead, it is easier to work with the effective Cauchy stress, that is obtained from the energy $W^h(\mathbf{F},\mathbf{H})$ by

$$\boldsymbol{\sigma} = \frac{1}{J}\frac{\partial w^h}{\partial \mathbf{F}}\bigg|_{\mathbf{h}}\mathbf{F}^T + \frac{1}{J}\left(\frac{\partial w^h}{\partial \mathbf{h}}\cdot\frac{\partial \mathbf{h}}{\partial \mathbf{F}}\right)\mathbf{F}^T \equiv \boldsymbol{\sigma}_{\texttt{mech}} + \boldsymbol{\sigma}_{\texttt{maxw}}. \tag{31}$$

Here, the first term is the purely mechanical stress, while the second part is the total average Maxwell Cauchy stress. Using next the second part of equation (30) and after some straightforward algebra and the chain rule (i.e. the fact that $\mathbf{h}$ depends on $\mathbf{H}$ and $\mathbf{F}$), we obtain

$$\begin{aligned}\boldsymbol{\sigma}_{\texttt{maxw}} = \frac{1}{J}\left(\frac{\partial w^h}{\partial \mathbf{h}}\cdot\frac{\partial \mathbf{h}}{\partial \mathbf{F}}\right)\mathbf{F}^T &= \frac{1}{J}\left[\left(\frac{\partial \phi^h}{\partial \mathbf{h}}\cdot\frac{\partial \mathbf{h}}{\partial \mathbf{F}}\right) - \frac{\mu_0}{2}J\frac{\partial(\mathbf{h}\cdot\mathbf{h})}{\partial \mathbf{h}}\frac{\partial \mathbf{h}}{\partial \mathbf{F}} - \frac{\mu_0}{2}\mathbf{h}\cdot\mathbf{h}\frac{\partial J}{\partial \mathbf{F}}\right]\mathbf{F}^T \\ &= \mu_0\mathbf{h}\mathbf{m} + \mu_0\mathbf{h}\mathbf{h} - \frac{\mu_0}{2}|\mathbf{h}|^2\mathbf{I} \\ &= \mathbf{h}\mathbf{b} - \frac{\mu_0}{2}|\mathbf{h}|^2\mathbf{I}.\end{aligned} \tag{32}$$

The mechanical and the Maxwell parts of the effective first Piola-Kirchhoff stress are then obtained via $\mathbf{S}_{\texttt{mech}} = J\boldsymbol{\sigma}_{\texttt{mech}}\mathbf{F}^{-T}$ and $\mathbf{S}_{\texttt{maxw}} = J\boldsymbol{\sigma}_{\texttt{maxw}}\mathbf{F}^{-T}$, respectively. Finally, the average mechanical traction at the boundary of the RVE in the reference configuration is given by (Danas, 2017)

$$\mathbf{T} = \left[\mathbf{S} - \mathbf{S}_{\texttt{maxw}}\right]\cdot\boldsymbol{\mathcal{N}} = \mathbf{S}_{\texttt{mech}}\cdot\boldsymbol{\mathcal{N}} \qquad \text{on} \qquad \partial\mathcal{V}_0^{\#}. \tag{33}$$

*3.2.1. An augmented variational principle*

This last boundary term allows us to analyze the pure microstructurally induced magneto-mechanical coupling in the RVE remaining free from any geometry/shape effects. Therefore, (33) is crucial in a coupled magneto-mechanical homogenization problem. The application of (33) in the homogenization problem (26) is, in turn, a non-trivial operation. Such operation necessitates the evaluation of $\mathbf{F}$, $\mathbf{S}$, $\mathbf{h}$, $\mathbf{b}$ and $\mathbf{m}$ from (26) followed by the application of (33). To avoid such iterations, an augmented variational principal (Danas, 2017), that is capable of applying the condition (33) directly to the homogenization problem, is employed.

Specifically, in order to apply the purely mechanical traction (33) on the boundaries of the RVE and also to ensure the continuity of the Maxwell stress $\mathbf{S}_{\texttt{maxw}}$ across the neighboring RVEs, one needs to deduct the average Maxwell energy, $W^H_{\texttt{maxw}}$, of the RVE from the homogenized energy (26). The latter is defined as

$$W^H_{\texttt{maxw}}(\mathbf{F},\mathbf{H}) = -\frac{\mu_0}{2}J\mathbf{F}^{-T}\mathbf{H}\cdot\mathbf{F}^{-T}\mathbf{H}, \tag{34}$$

and alone gives rise to a deformation gradient $\mathbf{F}$ under the application of $\mathbf{H}$ across the RVE. Thus, if it is not deducted from (26), one obtains a fictitious $\mathbf{F}$ in the RVE, even when non-magnetic phases (such as a simple polymer) are analyzed (Danas, 2017). In other words, the deduction of $W^H_{\texttt{maxw}}$ from $W^H$ upholds the practical condition of fixed, far-away magnets from the sample by not allowing the poles to move towards each other under an applied $h$-field $\mathbf{H}$. The energy $W^H$ in its original form (26), in turn, represents the electro-active homogenization problem, where the electrodes are attached directly on the sample.

As noted earlier, the magnetic poles create a uniform background magnetic field, which is indeed perturbed by the presence of the MRE sample by creating a self field around itself. Thus, a material point in the MRE sees a Eulerian $h$-field and not a Lagrangian which is the case in electroactive problems. The application of such an average Eulerian field as the loading in our homogenization problem can be achieved in various manners. The simplest and more practical way we follow in this work consists in constraining the product $\mathbf{F}^{-T}\mathbf{H} = \mathbf{h}$ to be equal to an *applied* average background $h$-field, denoted as $\mathbf{h}_a$.

The deduction of the average Maxwell energy, $W^H_{\mathtt{maxw}}$, defined in (34) together with the last constraint $\mathbf{F}^{-T}\mathbf{H} = \mathbf{h}_a$ are employed by the augmented variational principle (Danas, 2017)

$$\mathcal{P}^H(\mathbf{F},\mathbf{H}) = W^H(\mathbf{F},\mathbf{H}) + \frac{\mu_0}{2}J\mathbf{F}^{-T}\mathbf{H}\cdot\mathbf{F}^{-T}\mathbf{H} + \frac{\mu_0}{2\zeta}J|\mathbf{F}^{-T}\mathbf{H}-\mathbf{h}_a|^2 - \mathbf{S}_{\mathtt{mech}}\cdot(\mathbf{F}-\mathbf{I}). \tag{35}$$

Here, $W^H(\mathbf{F},\mathbf{H})$ is given by (30), $\zeta$ is a non-dimensional penalty factor serving to enforce the application of a Eulerian background $h-$field. In practice, it suffices to set it equal to a very small number left to be defined in Section 5.1. Also note that the last term in (35) should be dropped unless a non-zero average mechanical traction is applied.

It should be noted that the *mathematical* homogenization problem (26) is well posed and the additional terms in (35) are employed after solving for $W^H$ in (26). This is because the analytical estimates for $W^H$ are independent of the boundary conditions (Ponte Castañeda and Galipeau, 2011; Lopez-Pamies, 2014; Lefèvre and Lopez-Pamies, 2016a,b). However, the boundary condition (33) is crucial for the proper interpretation of the effective $\mathbf{F}$, $\mathbf{S}$, $\mathbf{h}$, $\mathbf{b}$ and $\mathbf{m}$ fields for a given RVE. For this reason, in the case of analytical homogenization or phenomenological modeling of an MRE, the function $W^H(\mathbf{F},\mathbf{H})$ is obtained explicitly or implicitly first, while the subtraction of $W^H_{\mathtt{maxw}}$ together with the application of the constraint $\mathbf{F}^{-T}\mathbf{H} = \mathbf{h}_a$ is be carried out *a posteriori* to extract the relevant estimates for $\mathbf{F}$, $\mathbf{S}$, $\mathbf{h}$, $\mathbf{b}$ and $\mathbf{m}$ of the MRE. In turn, in a numerical simulation of an RVE, that would require extremely long computation times since one has to obtain numerically the energy $W^H(\mathbf{F},\mathbf{H})$ and its derivatives. The augmented potential energy (35) offers a direct alternative allowing the direct evaluation of the desired estimates for $\mathbf{F}$, $\mathbf{S}$, $\mathbf{h}$, $\mathbf{b}$ and $\mathbf{m}$ under given loading conditions $\mathbf{h}_a$ and $\mathbf{T}$.

## 4. Exact and approximate solutions for the effective energy

In this section, we present two distinct families of theoretical models; an "implicit" one obtained by a rigorous homogenization analysis (Lefèvre and Lopez-Pamies, 2016a; Lefèvre et al., 2017) and "explicit" homogenization-guided phenomenological models, which are calibrated to recover the implicit homogenization estimates for a very large range of material parameters. In particular, motivated by microscopic images of standard MREs (Semisalova et al., 2013), we consider in this study only the case of spherical mechanically stiff but magnetically soft inclusions that are isotropically and uniformly distributed in a non-magnetic matrix phase. Nevertheless, the same ideas may apply to other composites such as polymers comprising ferrofluid inclusions (Lefèvre et al., 2017).

Specifically, in the original work of Lefèvre et al. (2017) estimates for both $W^H(\mathbf{F},\mathbf{H})$ and $W^B(\mathbf{F},\mathbf{B})$ were proposed. In the first case, an explicit estimate has been proposed for linear magnetic particles (i.e. linear local magnetic response of the particles such as the one given in equation (21)) and an implicit one for nonlinearly saturating ones. In turn, only an explicit model for linear magnetic particles has been proposed for $W^B(\mathbf{F},\mathbf{B})$, which resulted by a partial Legendre-Fenchel transform of the corresponding $W^H(\mathbf{F},\mathbf{H})$ model.

To fill this gap and simplify possible numerical implementations of such models in general purpose finite element codes, we propose next simple explicit energy densities $W^H(\mathbf{F},\mathbf{H})$ and $W^B(\mathbf{F},\mathbf{B})$ for nonlinearly saturating magnetic particles that are calibrated by using the analytical explicit and implicit homogenization models. Note, however, that the free parameters in the phenomenological models can be calibrated independently by available experiments or other numerical calculations, thus offering a well-designed yet simple energy description for MREs.

Finally, we discuss at the end of this section the finite element-based numerical simulations used to estimate the effective response of three-dimensional periodic RVEs. Those calculations, which are limited in the present study to fairly large matrix shear moduli due to the significant amount of computational time and sensitivity of calculations, are mainly used to assess the homogenization models.

Specifically, the analytical solutions of Lefèvre et al. (2017) consider an incompressible $I_1-$dependent matrix phase and mechanically rigid but magnetically soft particles without magnetic hysteresis. Thus, for the incompressible matrix phase, which is also magnetically inert (i.e., $\chi_{\mathtt{m}} = 0$), (12) along with (14) and (15) reduce to (Lefèvre et al., 2017)

$$W_{\mathtt{m}}(\breve{\mathbf{F}},\breve{\mathbf{H}}) = \begin{cases} \Phi^{\mathtt{mech}}_{\mathtt{m}}(\breve{I}_1) - \dfrac{\mu_0}{2}\breve{I}^H_5 & \text{if} \quad \breve{J}=1, \\ +\infty & \text{otherwise.} \end{cases} \tag{36}$$

In the special case of an incompressible Neo-Hookean material, $\Phi^{\mathtt{mech}}_{\mathtt{m}}(\breve{I}_1) = G_{\mathtt{m}}(\breve{I}_1-3)/2$, with $G_{\mathtt{m}}$ denoting the shear modulus of the matrix. In turn, the energy associated with the magneto-active mechanically rigid particles (i.e., with shear modulus $G_{\mathtt{p}} = +\infty$) is given by

$$W^H_p(\breve{\mathbf{F}},\breve{\mathbf{H}}) = \begin{cases} -\mathcal{S}_p(\breve{I}^H_5) & \text{if} \quad \breve{J}=1, \\ +\infty & \text{otherwise.} \end{cases} \tag{37}$$

where $I_5^H$ is the local invariant and has been defined in Table1, while the function $\mathcal{S}(I_5^H)$ is any nonlinear saturation function. In the present study, we report results for the Langevin-type saturation function defined in (15) for $\breve{J}=1$, such that

$$\mathcal{S}_{\mathrm{p}}(\breve{I}_5^H)=\frac{\mu_0}{2}\breve{I}_5^H+\frac{\mu_0(m_{\mathrm{p}}^s)^2}{3\chi_{\mathrm{p}}}\left\{\ln\left[\sinh\left(\frac{3\chi_{\mathrm{p}}}{m_{\mathrm{p}}^s}\sqrt{\breve{I}_5^H}\right)\right]-\ln\left[\frac{3\chi_{\mathrm{p}}}{m_{\mathrm{p}}^s}\sqrt{\breve{I}_5^H}\right]\right\}. \tag{38}$$

Here, $\chi_{\mathrm{p}}$ and $m_{\mathrm{p}}^s$ are the magnetic susceptibility and magnetization saturation of the particles, respectively.

### *4.1. Analytical homogenization solutions*

Given the above-described local energies for the matrix and the particle phase by (36) and (37), respectively, the homogenized energy reads (Lefèvre et al., 2017)

$$W^H(\mathbf{F},\mathbf{H})=\begin{cases}\Phi_{\mathtt{mech}}(\mathbf{F})-c\,\mathcal{S}_{\mathrm{p}}(\mathcal{I}_5^H)+\dfrac{c\,\xi}{2}\mathcal{I}_5^H+\dfrac{1}{2}\left(v\left(\xi\right)-z\left(\xi\right)\right)I_4^H-\dfrac{v\left(\xi\right)}{2}I_5^H & \text{if}\quad J=1\\ +\infty & \text{otherwise.}\end{cases} \tag{39}$$

In this expression, the purely mechanical effective energy is given by (Lopez-Pamies et al., 2013)

$$\Phi_{\mathtt{mech}}(\mathbf{F})=(1-c)\Phi_{\mathtt{m}}^{\mathtt{mech}}(\mathcal{I}_1), \tag{40}$$

where $\Phi_{\mathtt{m}}^{\mathtt{mech}}$ is defined in (14) for a Neo-Hookean material, $c$ denotes the particle volume fraction,

$$I_1=\mathrm{tr}(\mathbf{F}^T\mathbf{F}),\qquad I_4^H=\mathbf{H}\cdot\mathbf{H}=\mathbf{F}^T\mathbf{h}\cdot\mathbf{F}^T\mathbf{h},\qquad I_5^H=\mathbf{F}^{-T}\mathbf{H}\cdot\mathbf{F}^{-T}\mathbf{H}=\mathbf{h}\cdot\mathbf{h} \tag{41}$$

and

$$\mathcal{I}_1=\frac{I_1-3}{(1-c)^{7/2}}+3,\qquad \mathcal{I}_5^H=-\frac{54c(1-c)(\xi-\mu_0)\mu_0^2}{5[(2+c)\mu_0+(1-c)\xi]^3}I_4^H+\frac{9[(10-c+6c^2)\mu_0+(5+c-6c^2)\xi]\mu_0^2}{5[(2+c)\mu_0+(1-c)\xi]^3}I_5^H. \tag{42}$$

The effective coefficients $v(\xi)$ and $z(\xi)$ are given by

$$v(\xi)=\mu_0+\frac{3c(10+2c+3c^2)(\xi-\mu_0)\mu_0^2}{5[(2+c)\mu_0+(1-c)\xi]^2}+\frac{3c(1-c)(5+3c)(\xi-\mu_0)\mu_0\xi}{5[(2+c)\mu_0+(1-c)\xi]^2} \tag{43}$$

and

$$z(\xi)=\mu_0+\frac{3c\mu_0(\xi-\mu_0)}{[(2+c)\mu_0+(1-c)\xi]}, \tag{44}$$

respectively. The variables $v$ and $z$ depend also on $c$ and implicitly via $\xi$ on $\mathbf{F}$ and $\mathbf{H}$ but for the sake of clarity in the notation, we have omitted this dependence in the last two equations.

Then, the variable $\xi$ is defined implicitly as solution of the nonlinear algebraic equation[4]

$$2\mathcal{S}_{\mathrm{p}}'(\mathcal{I}_5^H)-\xi=0. \tag{45}$$

This last equation cannot be solved analytically for any standard nonlinear saturation function and thus implies that the term $\xi$ has *no* explicit expression in terms of the model parameters, rather, it has an implicit dependence on the $\mathbf{F}$ and $\mathbf{H}$ fields as well as on the volume fraction $c$ and the magnetic constants $\chi_{\mathrm{p}}$ and $m_{\mathrm{p}}^s$. Therefore, $W^H$ in (39) is an implicit function of $\mathbf{F}$ and $\mathbf{H}$.

For practical purposes, we recall the expressions used to evaluate the total stress $\mathbf{S}$ and Lagrangian magnetic field $\mathbf{B}$, i.e.,

$$\mathbf{S}=2(1-c)^{-5/2}\Phi_{\mathtt{m}}^{\mathtt{mech},\prime}(\mathcal{I}_1)\mathbf{F}+v(\xi)\mathbf{F}^{-T}\mathbf{H}\otimes\mathbf{F}^{-1}\mathbf{F}^{-T}\mathbf{H}-p\mathbf{F}^{-T}, \tag{46}$$

with $p$ indicating an arbitrary hydrostatic pressure arising from the incompressibility constraint $J=1$ and

$$\mathbf{B}=(z(\xi)-v(\xi))\mathbf{H}+v(\xi)\mathbf{F}^{-1}\mathbf{F}^{-T}\mathbf{H}. \tag{47}$$

Those expressions can be used appropriately to impose a Eulerian field $\mathbf{h}_a$ together with a purely mechanical traction as described in equation (33). In the following, it is necessary to remark two important limiting cases for equation (45).

**Remark 1.** In the limit of small $h$-fields and deformation gradients, i.e., $\bar{I}_4^H\to\bar{I}_5^H$ and $\bar{I}_5^H\to 0$ or equivalently $|\mathbf{H}|\to 0$ and $|\mathbf{FH}|\to 0$, $\mathcal{S}(\mathcal{I}_5^H)$ becomes linear in $\mathcal{I}_5^H$, which now reads $\mathcal{S}(\mathcal{I}_5^H)=\mu_{\mathrm{p}}\mathcal{I}_5^H/2$, with $\mu_{\mathrm{p}}=\mu_0(1+\chi_{\mathrm{p}})$ or equivalently $\xi=\mu_{\mathrm{p}}$. This linearization of $\mathcal{S}$ together with (45) leads to the effective magnetic permeability $\mu$ of the MRE at small magnetic fields, which reads

$$\mu=z(\mu_{\mathrm{p}})=\mu_0+\frac{3\,c\,\mu_0(\mu_{\mathrm{p}}-\mu_0)}{[(2+c)\mu_0+(1-c)\mu_{\mathrm{p}}]}\equiv(1+\chi)\mu_0, \tag{48}$$

[4]Throughout, we make use of the standard convention $g'(x)=\mathrm{d}g(x)/\mathrm{d}x$ to denote the derivative of functions of a single scalar variable.

while

$$v = v(\mu_{\mathrm{p}}) = \mu_0 + \frac{3c(10+2c+3c^2)(\mu_{\mathrm{p}}-\mu_0)\mu_0^2}{5[(2+c)\mu_0+(1-c)\mu_{\mathrm{p}}]^2} + \frac{3c(1-c)(5+3c)(\mu_{\mathrm{p}}-\mu_0)\mu_0\mu_{\mathrm{p}}}{5[(2+c)\mu_0+(1-c)\mu_{\mathrm{p}}]^2}. \tag{49}$$

Both $\mu$ and $v$[5] are of course independent of $\mathbf{F}$ and $\mathbf{H}$. In this last expression and for later use, we have also defined the effective susceptibility $\chi = \mu/\mu_0 - 1$ of the MRE. It is also noted that (48) corresponds to the well-known Maxwell-Garnett (or equivalently Hashin-Shtrikman) estimate for purely magnetic composites (Psarra et al., 2017). As a consequence, (39) may be expressed explicitly as

$$W_0^H(\mathbf{F},\mathbf{H}) = \begin{cases} \Phi_{\mathtt{mech}}(\mathbf{F}) + \dfrac{v-\mu}{2} I_4^H - \dfrac{v}{2} I_5^H & \text{if} \quad J=1 \\ +\infty & \text{otherwise.} \end{cases} \tag{50}$$

Here, the superscript 0 is used to denote the limiting case of $|\mathbf{H}| \to 0$, while the coefficient $v(\mu_{\mathrm{p}})$ is given by (49).

**Remark 2.** In the limit of very large magnetic fields, i.e., $|\mathbf{H}| \to \infty$, $\mathcal{S}(\mathcal{I}_5^H) = \mu_0 \mathcal{I}_5^H/2$ and hence $z = \xi = \mu_0$. In that same limit, the effective magnetization may be found to be simply

$$\mathbf{m} = m^s \frac{\mathbf{h}}{|\mathbf{h}|}, \qquad m^s = c\, m_{\mathrm{p}}^s, \tag{51}$$

which readily defines the effective saturation magnetization $m^s$ of the MRE. This result has also been confirmed numerically by Danas (2017) in the context of MREs, where the magnetization saturation of the MRE was shown to be independent of the microstructure itself but only function of the volume fraction of the particles.

These last two remarks are extremely important for proposing simple and consistent phenomenological models in the following sections.

*4.1.1. Explicit homogenization estimates for linear magnetic particles: F-B version*

Owing to the linearity of $W_0^H$ defined in (50) in the magneto-mechanical invariants $I_4^H$ and $I_5^H$, one can obtain the corresponding complimentary energy density $W_0^B(\mathbf{F},\mathbf{B})$ by application of the partial Legendre-Fenchel transform with respect to $\mathbf{H}$ (Bustamante and Ogden, 2012)

$$W^B(\mathbf{F},\mathbf{B}) = \sup_{\mathbf{H}} \left[\mathbf{B}\cdot\mathbf{H} + W^H(\mathbf{F},\mathbf{H})\right], \tag{52}$$

such that (Lefèvre et al., 2017)

$$W_0^B(\mathbf{F},\mathbf{B}) = \begin{cases} \Phi_{\mathtt{mech}}(\mathbf{F}) + \dfrac{1}{2v}\left[\dfrac{I_5^B + \eta^2 I_4^B + \eta(I_1 I_5^B - I_6^B)}{1+\eta^3+\eta^2 I_2 + \eta I_1}\right] & \text{if} \quad J=1 \\ +\infty & \text{otherwise,} \end{cases} \tag{53}$$

where the coefficient $\eta = (\mu - v)/v$ is introduced for convenience in the notation. In turn, $I_4^B$, $I_5^B$ and $I_6^B$ are the standard magneto-mechanical invariants in terms of $\mathbf{B}$ and in the incompressible limit $J=1$[6] are given by

$$I_4^B = \mathbf{B}\cdot\mathbf{B} = \mathbf{F}^{-1}\mathbf{b}\cdot\mathbf{F}^{-1}\mathbf{b}, \qquad I_5^B = \mathbf{F}\mathbf{B}\cdot\mathbf{F}\mathbf{B} = \mathbf{b}\cdot\mathbf{b} \qquad I_6^B = \mathbf{F}^T\mathbf{F}\mathbf{B}\cdot\mathbf{F}^T\mathbf{F}\mathbf{B} = \mathbf{F}\mathbf{b}\cdot\mathbf{F}\mathbf{b}, \tag{54}$$

respectively.

As it is evident from relation (53), $W_0^B$ exhibits a non-trivial coupling between purely mechanical and magneto-mechanical invariants. Nevertheless, by a closer inspection of the expression (53), we observe that the parameter $\eta$ is proportional to $\mu - v$, which is shown in Fig. 1a to be significantly smaller than unity for volume fractions $c \leq 0.3$ and magnetic permeabilities of particles $\mu_{\mathrm{p}}/\mu_0 < 50$. This observation allows us to approximate $W_0^B$ even further, an operation that will prove very useful in the next section where we propose explicit phenomenological models.

Thus, by neglecting higher order terms in $O(\eta^2)$ in (53), and keeping only the zero order term in $I_1 = 3 + O(|\mathbf{F}-\mathbf{I}|^2)$, we obtain the approximate energy density

$$W_0^B\big|_{|\eta|\ll 1}(\mathbf{F},\mathbf{B}) = \begin{cases} \Phi_{\mathtt{mech}}(\mathbf{F}) + \dfrac{1}{2v}\left[\dfrac{\tau\, I_5^B + \eta(3I_5^B - I_6^B)}{1+3\eta}\right] & \text{if} \quad J=1 \\ +\infty & \text{otherwise.} \end{cases} \tag{55}$$

[5] Henceforth, it is implied $v = v(\mu_{\mathrm{p}})$.

[6] The invariants $I_4^B$, $I_5^B$ and $I_6^B$ are all multiplied with $J^2$ in the case of compressible materials.

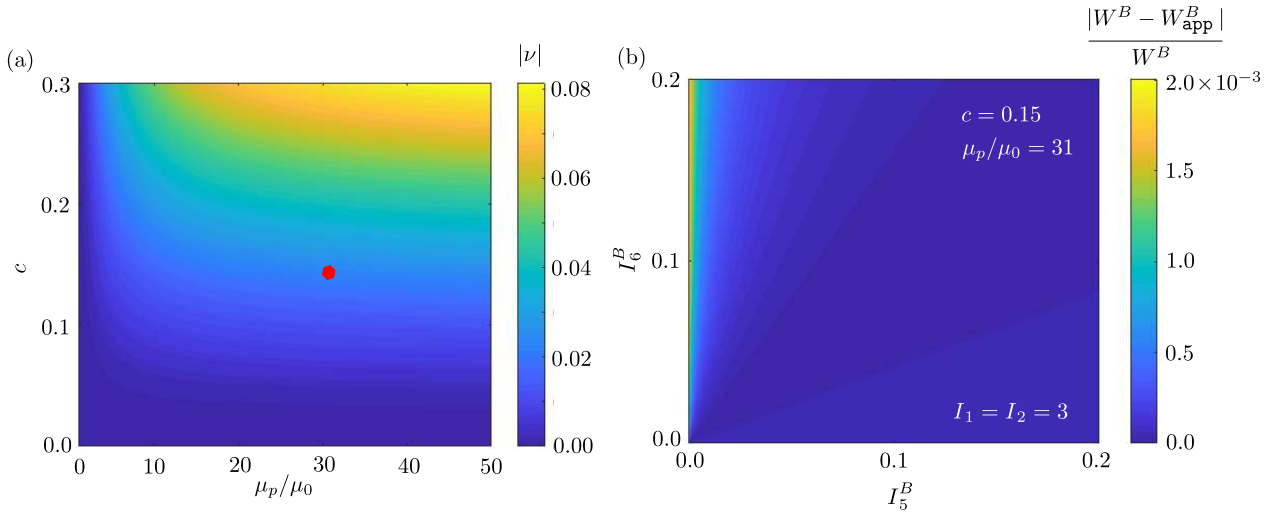


Figure 1: (a) Contour plot of the coefficient $\eta$ as a function of the particle volume fraction $c$ and the normalized magnetic permeability of the particles $\mu_{\mathtt{p}}/\mu_{\mathtt{0}}$. (b) Difference between the exact and approximate homogenization energy functions for a representative case of $c = 0.15$ and $\mu_{\mathtt{p}}/\mu_{\mathtt{0}} = 31$ indicated by a red point in part (a).

Here, the coefficient $\tau$ is introduced to ensure that the second term of (55) consistently leads to $I_5^B/2\mu$ in the limiting case of $|\mathbf{b}| \to 0$ and is consequently evaluated to be

$$\tau = \frac{5v\mu - 2v^2 - 2\mu^2}{v\mu} \tag{56}$$

after considering the limit $|\mathbf{b}| \to 0$ in (55). Finally, substitution of (56) into (55) leads to

$$W^B_{\mathtt{app}}(\mathbf{F},\mathbf{B}) = \begin{cases} \Phi_{\mathtt{mech}}(\mathbf{F}) + \dfrac{(v-\mu)}{2v(2v-3\mu)}(I_5^B - I_6^B) + \dfrac{1}{2\mu} I_5^B & \text{if} \quad J = 1 \\ +\infty & \text{otherwise,} \end{cases} \tag{57}$$

The approximate linearized energy (57) is compared with the original homogenized energy (53) in Fig. 1b. As is easily observed, the difference between those two estimates is very small and thus allows us to use expression (57) to obtain the initial response of the subsequent phenomenological model in the $\mathbf{F}-\mathbf{B}$ space in a straightforward manner. It is finally noted that all energies discussed in this section comprise the same purely mechanical part which is explicit and has been originally proposed in the work of Lopez-Pamies et al. (2013).

### *4.2. Microstructurally-guided explicit phenomenological models*

In this section, we propose fully explicit, homogenization-guided phenomenological models for the MRE using both $\mathbf{F}-\mathbf{H}$ and $\mathbf{F}-\mathbf{B}$ variables. The phenomenological models are proposed in terms of two additional modeling parameters, which are subsequently obtained via consistent linearization and fitting with the homogenized models. First, we propose models for incompressible MREs and then extend in an ad-hoc manner those models for nearly incompressible ones. This extension serves only practical purposes since it allows for a simpler numerical implementation. For consistency, we impose on the phenomenological model certain important properties, which are:

1. the phenomenological models shall have the same purely mechanical part with the homogenized models, i.e., $\Phi_{\mathtt{mech}}(\mathbf{F}) = (1-c)\Phi_{\mathtt{m}}^{\mathtt{mech}}(\mathcal{I}_1)$ with $\mathcal{I}_1$ given by (42).
2. for $\mathbf{H} = \mathbf{0}$ and arbitrary $\mathbf{F}$, both phenomenological models shall recover exactly the analytical homogenization solutions (50) and (57) for the $\mathbf{F}-\mathbf{H}$ and $\mathbf{F}-\mathbf{B}$ versions, respectively. This condition implies first that the phenomenological and homogenized models shall deliver the same initial magnetization response or equivalently give the same slope in the $\mathbf{b}-\mathbf{h}$ space, i.e., $\mu$ as defined from relation (48). And second, they both result in the same magnetostrictive response as $\mathbf{H} \to \mathbf{0}$ or whenever the magnetic particles are modeled as linear magnetic materials without saturation.
3. for $|\mathbf{H}| \to \infty$, both phenomenological and homogenized models shall lead to the same saturation magnetization response, i.e., $|\mathbf{m}| = m^s$ obtained in (51).

#### *4.2.1. Explicit F-H phenomenological model*

Given the above requirements, we propose a phenomenological energy function for incompressible MREs in terms of three distinct energy contributions, namely, a fully decoupled mechanical and magnetic energy and an additional coupling

energy, which reads

$$W^H(\mathbf{F},\mathbf{H}) = \begin{cases} \Phi_{\texttt{mech}}(\mathbf{F}) + \Phi^H_{\texttt{mag}}(I_5^H) + \Phi^H_{\texttt{couple}}(I_4^H, I_5^H) - \dfrac{\mu_0}{2} I_5^H & \text{if} \quad J = 1 \\ +\infty & \text{otherwise,} \end{cases} \tag{58}$$

where the effective mechanical energy $\Phi_{\texttt{mech}}$ is given by (40), and $I_4^H$ and $I_5^H$ by (41). Instead, the *purely* magnetic part $\Phi_{\texttt{mag}}$ is given in terms of a Gaussian Hypergeometric function, denoted by ${}_2\mathcal{F}_1$, as

$$\begin{aligned} \Phi^H_{\texttt{mag}}(I_5^H) &= -\frac{\mu_0}{2}\chi I_5^H \, {}_2\mathcal{F}_1\left[\frac{1}{k^H}, \frac{2}{k^H}, 1+\frac{2}{k^H}, -\left(\frac{\chi\sqrt{I_5^H}}{m^s}\right)^{k^H}\right], \\ &= -\frac{\mu_0}{2}\chi |\mathbf{h}|^2 \, {}_2\mathcal{F}_1\left[\frac{1}{k^H}, \frac{2}{k^H}, 1+\frac{2}{k^H}, -\left(\frac{\chi\,|\mathbf{h}|}{m^s}\right)^{k^H}\right] = \phi^h_{\texttt{mag}}(\mathbf{h}). \end{aligned} \tag{59}$$

In this expression, $k^H$ is a positive integer, $m^s = c\, m^s_{\texttt{p}}$ denotes the effective saturation magnetization and $\chi = (\mu/\mu_0 - 1)$ is the effective magnetic susceptibility, which is given by (48). The function ${}_2\mathcal{F}_1$ is typically expressed in terms of a series given by,

$${}_2\mathcal{F}_1[a,b,c;z] = \sum_{n=0}^{\infty} \frac{(a)_n (b)_n}{(c)_n} \frac{z^n}{n!}, \tag{60}$$

with

$$(x)_0 = 1 \qquad \text{and} \qquad (x)_n = x(x+1)\cdots(x+n-1).$$

It can be shown via rigorous convergence tests that the infinite series in (60) converge for all $z < 0$ and non-negative $a$, $b$ and $c$ (Abramowitz and Stegun, 1972, p. 81-86). Hence, (60) can be evaluated numerically in a straightforward manner (Perger et al., 1993; Hankin, 2015). Of interest, however, are the first and second derivatives of $\phi^h_{\texttt{mag}}(\mathbf{h})$ with respect to $\mathbf{h}$, which, as shown in the following, take very simple algebraic forms.

Subsequently, motivated by the corresponding homogenized model in equation (39), we express the coupled magneto-mechanical energy as a function of the two invariants $I_4^H$ and $I_5^H$, thus taking the form

$$\Phi^H_{\texttt{couple}}(I_4^H, I_5^H) = \Phi^H_4(I_4^H) - \Phi^H_5(I_5^H), \tag{61}$$

with

$$\Phi^H_i(I_i^H) = \beta_1^H \frac{\mu_0 (m^s)^2}{2\chi} \ln\left[1 + \sum_{q=1}^{4} \frac{1}{c}\left(\frac{4}{5}\chi\right)^{q+1} \left(\frac{c}{\beta_2^H}\right)^q \left(\frac{\sqrt{I_i^H}}{m^s}\right)^{2q}\right], \qquad i = 4, 5. \tag{62}$$

In the above expressions, we have introduced three free parameters, namely, $k^H$, $\beta_1^H$ and $\beta_2^H$. The evaluation and selection of these parameters using the analytical homogenization model in (39) is described in detail in the following.

*The selection of the parameter $k^H$.* We start by noting that the derivative of the Gaussian Hypergeometric function ${}_2\mathcal{F}_1$ with respect to its argument has a very simple form, which reads

$$\mathbf{m} = -\frac{1}{\mu_0}\frac{\partial \phi^h_{\texttt{mag}}}{\partial \mathbf{h}} = \frac{\chi \mathbf{h}}{\left[1 + (\chi)^{k^H} \left(|\mathbf{h}|/m^s\right)^{k^H}\right]^{1/k^H}}. \tag{63}$$

Here, the initial susceptibility is always $\chi$ irrespective of the value of $k^H$ thus leading to the correct (in the sense of homogenization) initial effective magnetization response of the MRE. The same is true for the saturation response, which gives $|\mathbf{m}| = m^s$ as required by the homogenization process. On the other hand, the rate of magnetization depends on the power coefficient $k^H$, which may be calibrated to follow closely the homogenized response. Specifically, by direct calibration, we find in Section 5 that a value

$$k^H = 4 \tag{64}$$

leads to a good fit for the magnetization response for all volume fractions $c \in [0, 0.3]$ and matrix shear moduli analyzed in the present study. Of course, given any experimental data, a different value for $k^H$ may be used. For illustration purposes, we show in Fig. 2 representative curves of the hypergeometric function and its derivative, which gives the $\mathbf{m}-\mathbf{h}$ response as evaluated from equation (63). For comparison, magnetization curves obtained by the Langevin (based on definition (16)) and the hyperbolic tangent functions (see equations (2.12) and (2.14) in Danas (2017)) are also shown. The use of a hypergeometric function is done in order to allow for flexibility in the calibration process since the homogenized response of an MRE comprising magnetic particles with Langevin-type magnetization saturation response does not lead to an effective magnetization response of a Langevin-type, as is discussed in Section 5. Before proceeding to the coupled energy part, we note further that the decoupled mechanical and magnetic energies are expressed in terms of the homogenized material parameters, which can be evaluated directly in terms of the constituents' properties and the particle volume fraction $c$.

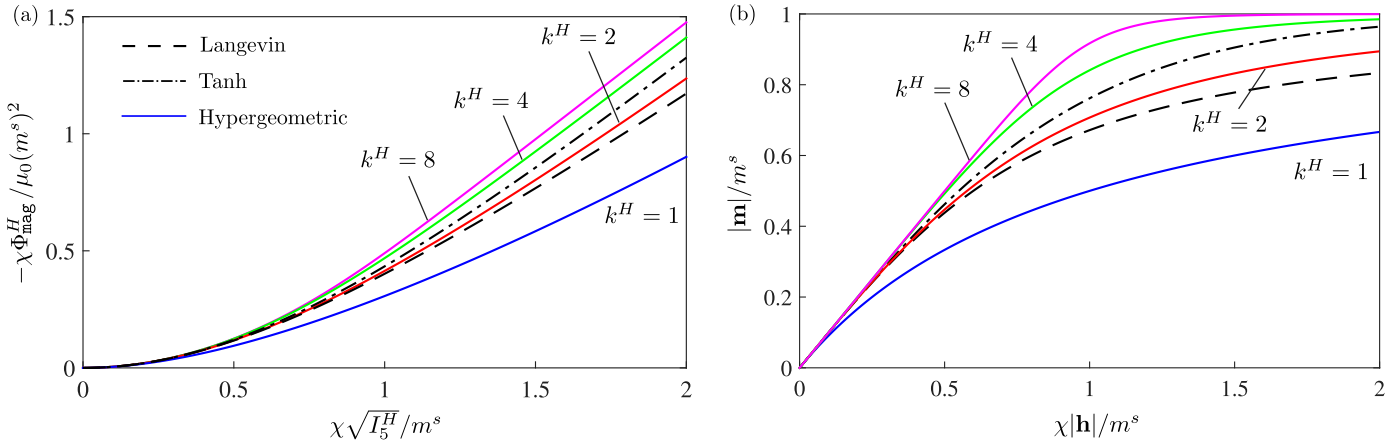


Figure 2: Comparison of (a) the magnetic energy functions and of (b) their derivatives obtained from and hypergeometric $\Phi^h_{\mathtt{mag}}$ saturation function given in equation (63) for various exponents $k^H$, the Langevin function (based on definition (15)) and the hyperbolic tangent function (see equations (2.12) and (2.14) in Danas (2017)).

*The evaluation of the parameter* $\beta_1^H$. To facilitate the relevant discussion, we show in Fig. 3 the response of $\Phi_i^H$ as a function of the invariant $I_i^H$. First, we observe that $\Phi_i^H$ is non-convex with respect to $\sqrt{I_i^H}$ since its derivative increases rapidly from zero to a maximum and then gradually decreases to zero (see Fig. 3b). As we will see in the following, such a function allows to obtain a material magnetostriction response that is initially quadratic, subsequently increases in a non-quadratic manner until finally reaching a saturating state.

Another important comment is related to the specific form of $\Phi^H_{\mathtt{couple}}$, i.e., the subtraction term $\Phi_4^H(I_4^H) - \Phi_5^H(I_5^H)$. This is done for two reasons. First, the derivation of $\Phi^H_{\mathtt{couple}}$ with respect to $\mathbf{h}$ leaves the magnetization response completely unaffected at small and very large applied magnetic fields $\mathbf{h}_a$, thus allowing the hypergeometric function in equation (59) to completely control the $\mathbf{m} - \mathbf{h}$ response at the initial regime and the saturation regime. The second reason is that only the $I_4^H = \mathbf{F}^T\mathbf{h}\cdot\mathbf{F}^T\mathbf{h}$ part of the function contributes to the magnetostriction whenever a Eulerian field $\mathbf{h}_a$ is applied, while the corresponding $I_5^H = \mathbf{h}\cdot\mathbf{h}$ part induces no magnetostriction.

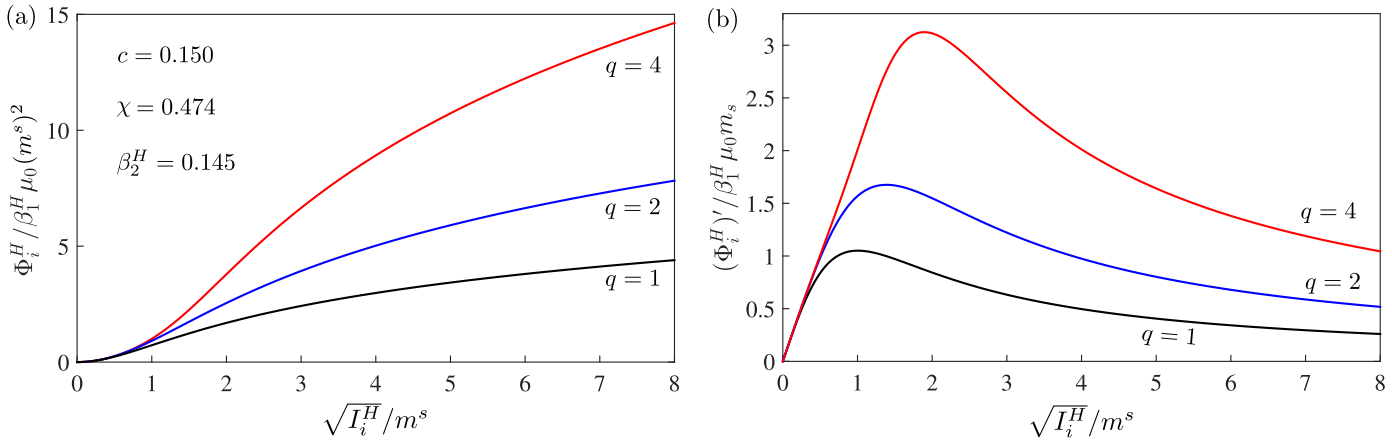


Figure 3: Representative plots of (a) the function $\Phi_i^H$ (with $i = 4, 5$) and (b) of its derivative with respect to $\sqrt{I_i^H}$ for $q = 1, 2, 4$.

In view of the above observations, the evaluation of $\beta_1^H$ is readily obtained by enforcing an exact equivalence between the phenomenological model (58) and the linearized homogenized model (39) in the limit of $|\mathbf{h}| \to 0$. To achieve that, we expand $W^H$ in equation (58) around $I_4^H = I_5^H = 0$, to obtain

$$W_0^H(\mathbf{F},\mathbf{H}) = \begin{cases} \Phi_{\mathtt{mech}}(\mathcal{I}_1) + 16\dfrac{(\mu-\mu_0)}{50}\dfrac{\beta_1^H}{\beta_2^H}(I_4^H - I_5^H) - \dfrac{\mu}{2}I_5^H & \text{if} \quad J = 1 \\ +\infty & \text{otherwise.} \end{cases} \tag{65}$$

By direct matching of the individual coefficients of $I_4^H$ and $I_5^H$ in (65) with those in (50), one gets

$$\beta_1^H = \frac{25}{16}\frac{(\nu-\mu)}{(\mu-\mu_0)}\beta_2^H. \tag{66}$$

The above definition of $\beta_1^H$ ensures that the initial (quadratic) magnetostriction obtained from the homogenization model (39) and the phenomenological model (58) is exactly the same. Evidently, (65) becomes independent of $\beta_2^H$ after substitution of (66) for $\beta_1^H$.

*The selection of the parameter* $\beta_2^H$. The parameter $\beta_2^H$ affects the magnetostriction response at larger $h$-fields as a result of the nonlinearity of the coupled function $\Phi^H_{\texttt{couple}}$ in (61) but not the initial magnetostriction. Therefore, the parameter $\beta_2^H$ needs to be calibrated numerically by fitting the magnetostriction response of the phenomenological model with that of the homogenized model (39) at large $\mathbf{h}$. It is worth noting here that the numerical fitting process is carried out by considering a zero applied mechanical traction (see equation (33)) and a Eulerian applied $h$-field $\mathbf{h}_a$, as discussed in Section 3.2. To achieve that, we employ the least square-based curve fitting algorithm `lsqurvefit` of MATLAB.

More specifically, the coupling coefficient $\beta_2^H$ essentially depends on four material parameters: the shear modulus $G_{\mathtt{m}}$ of the matrix, the initial susceptibility $\chi_{\mathtt{p}}$, the saturation magnetization $m^s_{\mathtt{p}}$ of the particles and the particle volume fraction $c$. In practice, most of the MREs are fabricated by curing the commercially available carbonyl iron particles along with various elastomers in different proportions (Danas et al., 2012; Psarra et al., 2017; Bodelot et al., 2018). Therefore, $G_{\mathtt{m}}$ and $c$ are the two key parameters[7] that vary for different MRE samples, while we set $\chi_{\mathtt{p}} = 30$ and $\mu_0 m^s_{\mathtt{p}} = 2.5$T, as obtained experimentally in Psarra et al. (2017).

First, we observe that $\beta_2^H$ becomes almost independent of $G_{\mathtt{m}}$ and $c$ for $G_{\mathtt{m}} > 1$MPa. Hence, we introduce a non-dimensional shear modulus, $G^*_{\mathtt{m}} = G_{\mathtt{m}}/G^{\mathtt{Ref}}_{\mathtt{m}}$, where $G^{\mathtt{Ref}}_{\mathtt{m}} = 1$MPa. The fitting process then involves scanning for the optimum $\beta_2^H$ in the $0.001 \leq G^*_{\mathtt{m}} \leq 1.5$ and $0 < c \leq 0.3$ range, as shown in Fig. 4a. The fitting of the contour in that

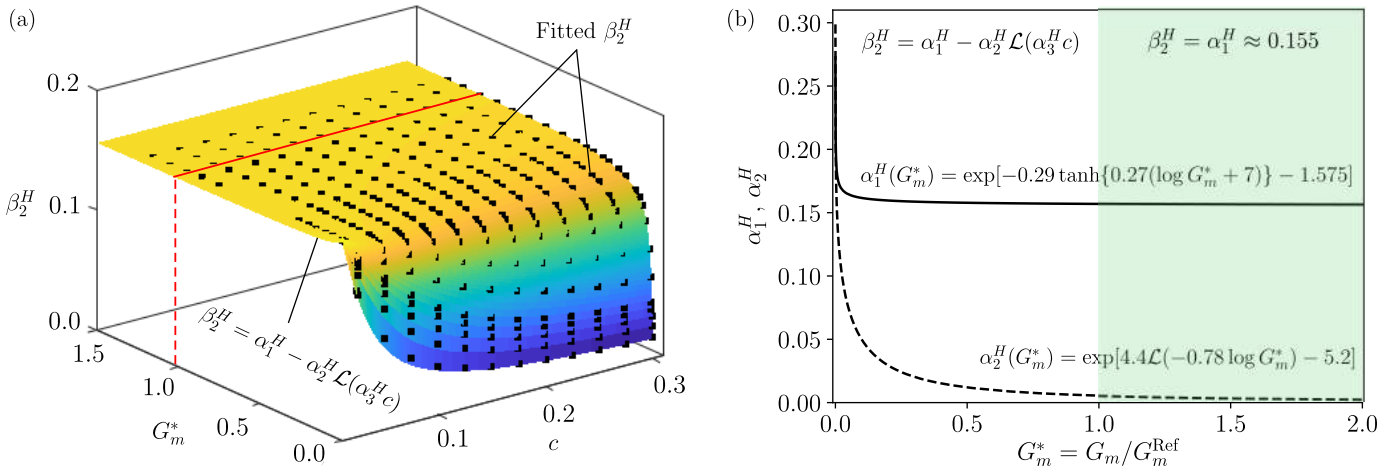


Figure 4: (a) Calibrated $\beta_2^H(G^*_{\mathtt{m}}, c)$ in the $G^*_{\mathtt{m}} - c$ space with the smooth surface showing the profile of the function (67) for $\beta_2^H(G^*_{\mathtt{m}}, c)$ and the black dots representing the optimized $\beta_2^H$ as obtained via fitting the magnetostriction response with the analytical homogenization model. (b) Evolution of the functions $\alpha_1^H(G^*_{\mathtt{m}})$ and $\alpha_2^H(G^*_{\mathtt{m}})$ in (67) with $G^*_{\mathtt{m}}$.

figure gives

$$\beta_2^H(G^*_{\mathtt{m}}, c) = \alpha_1^H(G^*_{\mathtt{m}}) - \alpha_2^H(G^*_{\mathtt{m}})\mathcal{L}\big[c\,\alpha_3^H(G^*_{\mathtt{m}})\big], \tag{67}$$

with

$$\begin{aligned}
\alpha_1^H(G^*_{\mathtt{m}}) &= \exp\big[-0.29\tanh\big\{0.27(\ln G^*_{\mathtt{m}} + 7)\big\} - 1.575\big],\\
\alpha_2^H(G^*_{\mathtt{m}}) &= \exp\big[4.4\mathcal{L}(-0.78\ln G^*_{\mathtt{m}}) - 5.2\big],\\
\alpha_3^H(G^*_{\mathtt{m}}) &= \frac{0.1}{G^*_{\mathtt{m}} + 0.0007} - 5.4G^*_{\mathtt{m}} + 6.75.
\end{aligned}$$

Here, $\mathcal{L}(.)$ is the Langevin function given by (16). Specifically, the evolution of $\beta_2^H$ with respect to $G^*_{\mathtt{m}}$ is mainly controlled by the coefficients $\alpha_1^H$ and $\alpha_2^H$. In turn, the third coefficient $\alpha_3^H$ is used to model the variation of $\beta_2^H$ with respect to $c$ for a given $G^*_{\mathtt{m}}$. The dependence of the functions $\alpha_1^H$ and $\alpha_2^H$ on $G^*_{\mathtt{m}}$ is shown in Fig. 4b, where we observe that $\alpha_2^H \approx 0$ for $G^*_{\mathtt{m}} > 1$, i.e., for all $G_{\mathtt{m}} > G^*_{\mathtt{m}}$. Hence, beyond $G^*_{\mathtt{m}} > 1$ a constant $\beta_2^H \approx 0.155$ is sufficient. On the other hand, for very soft, gel-like MREs, i.e., in the range of $0.01 \leq G^*_{\mathtt{m}} \leq 0.001$, the coupling coefficient $\beta_2^H$ becomes highly sensitive to $G^*_{\mathtt{m}}$ and $c$, resulting in a significant variation of $\beta_2^H$ in this particular range (see Fig.4a).

**Remark 3.** In spite of the fact that the assumption of an incompressible matrix and rigid particles leads to very efficient analytical estimates of the effective response, compressible models for the MREs are employed in most of the computational investigations due to their simplicity to incorporate them in a finite-element solver. Unfortunately, carrying out the homogenization problem for a compressible matrix is extremely difficult and no rigorous model is available up to

[7]Different values of $\chi_{\mathtt{p}}$ and $m^s_{\mathtt{p}}$ are expected to change the functions obtained below but only weakly, whereas one can always find the optimal coefficient $\beta_2^H$ by simply fitting the homogenized model for the given set of material properties of interest.

date neither for the purely mechanical part nor for the magneto-mechanical part. In this regard, we propose an ad-hoc extension of the incompressible phenomenological model (58) that essentially relaxes the assumption of incompressibility without affecting the aforementioned key features of the model at least in the case of high bulk modulus (i.e. nearly incompressible materials). The proposed compressible model reads

$$W^H_{\texttt{comp}}(\mathbf{F},\mathbf{H}) = \Phi^{\texttt{comp}}_{\texttt{mech}}(\mathcal{I}_1, J) + \Phi^H_{\texttt{mag}}(I^H_5) + \Phi^H_{\texttt{couple}}(I^H_4, I^H_5) - \frac{J\,\mu_0}{2} I^H_5, \tag{68}$$

where

$$\Phi^{\texttt{comp}}_{\texttt{mech}}(\mathcal{I}_1, J) = \Phi_{\texttt{mech}}(\mathcal{I}_1) - \frac{G_{\texttt{m}}}{(1-c)^{5/2}} \ln J + \frac{G'_{\texttt{m}}}{2(1-c)^6}(J-1)^2. \tag{69}$$

where $\Phi_{\texttt{mech}}$ and $\mathcal{I}_1$ have been defined in (40) and (42), respectively, whereas $G'_{\texttt{m}}$ is the Lamé constant associated with the compressibility modulus of the matrix. A nearly incompressible response is obtained for values $G'_{\texttt{m}} \geq 100 G_{\texttt{m}}$, which is the key assumption in most of the numerical computations associated with MREs. In that range, we observe no visible difference between the incompressible and the nearly incompressible versions for both the magnetostriction and the magnetization response.

*4.2.2. Explicit F-B phenomenological model*

In principle, one can obtain an equivalent F-B model via the partial Legendre-Fenchel transformation (52) of (58) with respect to $\mathbf{H}$. However, due to the severe nonlinearity of the functions associated with the proposed F-H model (58), one can not obtain its complementary energy in an explicit form. Instead, a complementary energy $W^B$, which has the exact same form as that of $W^H$ in (58), is proposed directly as

$$W^B(\mathbf{F},\mathbf{B}) = \begin{cases} \Phi_{\texttt{mech}}(\mathbf{F}) + \Phi^B_{\texttt{mag}}(I^B_5) + \Phi^B_{\texttt{couple}}(I^B_5, I^B_6) + \dfrac{1}{2\mu_0} I^B_5 & \text{if} \quad J = 1 \\ +\infty & \text{otherwise,} \end{cases} \tag{70}$$

where the magneto-mechanical invariants $I^B_5$ and $I^B_6$ have been defined in (54). Evidently, the first term of (70) that represents the purely mechanical component of $W^B$ is identical to that in (39) and (58), and is given by (40). Also, the last term of (70) represents the F-B version of the magnetostatic energy of free space (Dorfmann and Ogden, 2004).

It remains then to prescribe the two free energies, namely, the magnetic and the coupled free energy. Due to their intrinsic properties, $\Phi^B_{\texttt{mag}}$ and $\Phi^B_{couple}$ retain the same functional form to their F-H counterparts (59) and (61), respectively. Note that, as shown in Figs. 2 and 3, the hypergeometric ${}_2\mathcal{F}_1$ and the $\Phi^H_i$ functions are rich enough to model a wide variety of constitutive responses.

In this regard, the purely magnetic part $\Phi^B_{\texttt{mag}}$ is chosen as

$$\begin{aligned} \Phi^B_{\texttt{mag}}(I^B_5) &= -\frac{\chi}{2\mu_0\,(1+\chi)} I^B_5\, {}_2\mathcal{F}_1\left[\frac{1}{k^B}, \frac{2}{k^B}, 1+\frac{2}{k^B}, -\left(\frac{\chi\sqrt{I^B_5}}{(1+\chi)\mu_0 m^s}\right)^{k^B}\right] \\ &= -\frac{\chi}{2\mu_0\,(1+\chi)} |\mathbf{b}|^2\, {}_2\mathcal{F}_1\left[\frac{1}{k^B}, \frac{2}{k^B}, 1+\frac{2}{k^B}, -\left(\frac{\chi\,|\mathbf{b}|}{(1+\chi)\mu_0 m^s}\right)^{k^B}\right] = \phi^b_{\texttt{mag}}(\mathbf{b}), \end{aligned} \tag{71}$$

while, the coupling energy is defined by

$$\Phi^B_{\texttt{couple}}(I^B_5, I^B_6) = \Phi^B_6(I^B_6) - \Phi^B_5(I^B_5), \;\; \text{with} \;\; \Phi^B_i(I^B_i) = \beta^B_1 \frac{(1+\chi)\mu_0 (m^s)^2}{2\chi} \ln\left[1 + \sum_{q=1}^{4} \frac{1}{c}\left(\frac{5}{4}\frac{\chi}{1+\chi}\right)^{q+1} \left(\frac{c}{\beta^B_2}\right)^q \left(\frac{\sqrt{I^B_i}}{\mu_0 m^s}\right)^{2q}\right], \tag{72}$$

where $i = 5, 6$ and again $m^s = c\, m^s_{\texttt{p}}$.

**Remark 4.** As stated earlier, (72) retains an identical functional form as its F-H counterpart in (61) except that the magneto-mechanical coupling is now modeled in terms of the invariant $I^B_6$. This choice of the coupling invariant is not arbitrary, rather, is directly equivalent to the F-H model. The invariant $I^H_4$ in the F-H model can be expressed in terms of the Eulerian $\mathbf{h}$ as $I^H_4 = \mathbf{F}^T\mathbf{h} \cdot \mathbf{F}^T\mathbf{h}$. The Legendre-Fenchel transform of that invariant leads to the invariant $I^B_6 = \mathbf{F}^T\mathbf{b} \cdot \mathbf{F}^T\mathbf{b}$. In addition, and perhaps more importantly, we have shown that in the linearized regime, the corresponding homogenized model (53) can be approximated accurately by the model in (57), which in turn depends on $I^B_5$ and $I^B_6$.

In expressions (71) and (72), we have introduced three free parameters, namely, $k^B$, $\beta^B_1$ and $\beta^B_2$. The evaluation and selection of these parameters using the analytical homogenization model defined in (39) as well as the approximate linearized one in (57) is described in detail in the following.

*The selection of the parameter $k^B$.* Similar to the F-H version, a single exponent

$$k^B = 6 \tag{73}$$

provides a good fit to the magnetization response for all particle volume fractions and matrix shear moduli considered in this study. Note that the purely magnetic energy (71) in the F-B model is *not* an exact Legendre transform of the corresponding magnetic energy (59) of the F-H model. Thus, no direct correlation can be drawn between the model parameters $k^B$ and $k^H$ and their calibration values.

*The evaluation of the parameter* $\beta_1^B$. The evaluation of the coefficient $\beta_1^B$ is carried out in a similar fashion (i.e., via consistent linearization and fitting with the homogenized response) to the F-B homogenization model. In the limit of small $|\mathbf{b}| \to 0$, (70) can be expanded in terms of the invariants around $I_i^B = 0$ (with $i = 5, 6$). Thus, retaining only the leading order terms in $I_i^B$, one can express (70) as

$$W_0^B(\mathbf{F}, \mathbf{B}) = \begin{cases} \Phi_{\mathtt{mech}}(\mathbf{F}) + \dfrac{25}{32}\dfrac{\beta_1^B}{\beta_2^B}\dfrac{(\mu - \mu_0)}{\mu\mu_0}(I_6^B - I_5^B) + \dfrac{1}{2\mu}I_5^B & \text{if} \quad J = 1 \\ +\infty & \text{otherwise.} \end{cases} \tag{74}$$

By direct matching of this last free energy function with the approximate linearized one defined in equation (57), we obtain

$$\beta_1^B = \frac{16}{25}\frac{\mu_0\mu(v - \mu)}{v(\mu - \mu_0)(3\mu - 2v)}\beta_2^B. \tag{75}$$

The above relation for $\beta_1^B$ ensures that the initial (quadratic) magnetostriction obtained from the homogenization model (57) and the phenomenological model (70) is exactly the same. Evidently, (74) becomes independent of $\beta_2^B$ after substitution of (75) for $\beta_1^B$.

*The selection of the parameter* $\beta_2^B$. The parameter $\beta_2^B$ affects the magnetostriction response at larger $h$-fields as a result of the nonlinearity of the coupled function $\Phi_{\mathtt{couple}}^B$ in (72). Thus, the F-B phenomenological model is also reduced to a single modeling parameter, $\beta_2^B$. This parameter is then obtained by fitting the material magnetostriction obtained from the phenomenological model (70) with that from the homogenization model (39). The optimal $\beta_2^B$ for a given $G_{\mathtt{m}}^*$ and $c$ is shown by black squares in Fig. 5, which is qualitatively similar to Fig. 4a. For convenience in the notation, here we use the same non-dimensional shear modulus $G_{\mathtt{m}}^*$ as defined in Section 4.2.1. Specifically, we use two piecewise

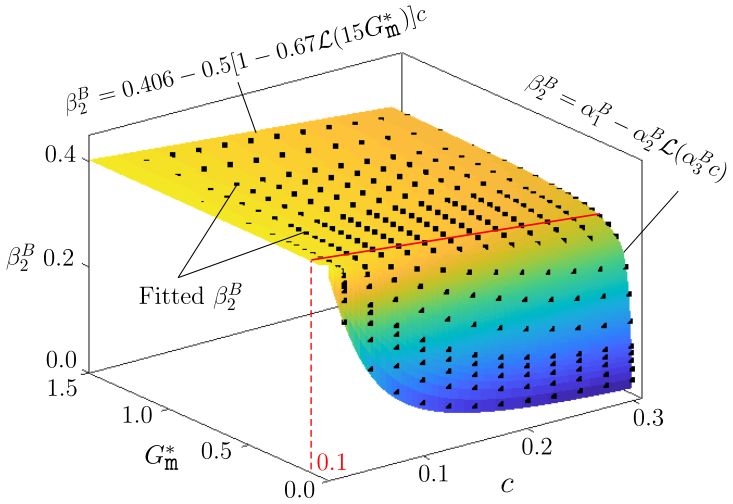


Figure 5: Calibrated $\beta_2^B(G_{\mathtt{m}}^*, c)$ in the $G_{\mathtt{m}}^* - c$ space with the smooth surface showing the profile of the function (76) for $\beta_2^B(G_{\mathtt{m}}^*, c)$ and the black dots representing the optimized $\beta_2^B$ as obtained via fitting the magnetostriction response with the analytical homogenization model.

continuous functions of $G_{\mathtt{m}}^*$ and $c$ to model the variation of $\beta_2^B$ in the $G_{\mathtt{m}}^* - c$ space, which reads

$$\beta_2^B(G_{\mathtt{m}}^*, c) = \begin{cases} \alpha_1^B(G_{\mathtt{m}}^*) - \alpha_2^B(G_{\mathtt{m}}^*)\mathcal{L}\big[c\,\alpha_3^B(G_{\mathtt{m}}^*)\big], & \text{if} \quad G_{\mathtt{m}}^* \le 0.1 \\ 0.4055 - 0.5\,c\,\big[1 - 0.67\mathcal{L}(15G_{\mathtt{m}}^*)\big] & \text{otherwise} \end{cases} \tag{76}$$

with

$$\begin{aligned} \alpha_1^B(G_{\mathtt{m}}^*) &= \exp\big[-0.029\ln G_{\mathtt{m}}^* - 0.982\big], \\ \alpha_2^B(G_{\mathtt{m}}^*) &= \exp\big[1.78\mathcal{L}(-0.32\ln G_{\mathtt{m}}^*) - 1.78\big], \\ \alpha_3^B(G_{\mathtt{m}}^*) &= \exp\big[0.14 - 0.54\ln G_{\mathtt{m}}^*\big]. \end{aligned}$$

Here, $\mathcal{L}(.)$ is again the Langevin function defined in (16). The first function is similar to $\beta_2^H$ with three coefficients $\alpha_1^B$, $\alpha_2^B$ and $\alpha_3^B$, which are functions of $G_{\mathtt{m}}^*$, whereas, the second function, which models $\beta_2^B$ for all $G_{\mathtt{m}}^* > 0.1$, is rather a simple function of $G_{\mathtt{m}}^*$ and $c$. We observe in Fig. 5 that the two fitting functions for $\beta_2^B$ have approximately the same magnitude near $G_{\mathtt{m}}^* = 0.1$. Thus, the particular choice of piecewise continuous $\beta_2^B$ ensures a constant transition from the Langevin decay to the linear decrease regime.

**Remark 5.** A compressible version of (70) is given by

$$W^B_{\texttt{comp}}(\mathbf{F},\mathbf{B}) = \Phi^{\texttt{comp}}_{\texttt{mech}}(\mathcal{I}_1, J) + \Phi^B_{\texttt{mag}}\left(\frac{I^B_5}{J^2}\right) + \Phi^B_{couple}\left(\frac{I^B_5}{J^2}, \frac{I^B_6}{J^4}\right) + \frac{1}{2\mu_0 J} I^B_5, \tag{77}$$

where $\Phi^{\texttt{comp}}_{\texttt{mech}}$ is given by (69).

### *4.3. Numerical computations of the effective response*

The effective response and specifically the average magnetostriction and magnetization of the MRE is also evaluated numerically by employing the augmented variational principle (35) similar to the study of Danas (2017) and Keip and Sridhar (2018). To accomplish this, we employ a standard nonlinear finite-element framework to numerically evaluate the local $\breve{\mathbf{F}}$ and $\breve{\mathbf{H}}$ fields in a periodic RVE. The finite-element framework requires a well-defined geometry with a suitable mesh. For the magnetostrictive two-phase composites at hand, we consider a three dimensional cubic periodic RVE, which occupies a reference volume of $\mathcal{V}_0^{\#} = L^3$. We then generate a random distribution of non-overlapping spherical particles of different size in the RVE using the random sequential adsorption (RSA) algorithm (Rintoul and Torquato, 1997; Segurado and Llorca, 2002; Anoukou et al., 2018; Zerhouni et al., 2019). For efficient meshing and to avoid excessive mesh distortions, the minimum distance between two particles is considered to be 1.05 times the average diameter of the two particles. Moreover, a particle position is also rejected if it lies very close to the edge of the RVE. These two conditions give a sufficiently easy-to-mesh 3D particle-filled RVE.

Periodic boundary conditions are applied across the RVEs by constraining suitably the nodal displacement $\breve{\mathbf{u}}(\mathbf{X})$ and scalar potential $\breve{\varphi}(\mathbf{X})$ fields at the boundary and the corner nodes of the RVE as discussed extensively in Danas (2017) and Keip and Rambausek (2015). Note from (27) and (28) that all the admissible $\breve{\mathbf{u}}$ and $\breve{\varphi}$ can be additively decomposed into their average field $\mathbf{u}$ and $\varphi$ and periodic perturbations $\widetilde{\mathbf{u}}$ and $\widetilde{\varphi}$, respectively. Owing to their periodicity in space, the perturbation fields $\widetilde{\mathbf{u}}$ and $\widetilde{\varphi}$ assume the same value on the opposite boundary/corner nodes of the cubic RVE. By exploiting these periodicity conditions one can constrain the $\breve{\mathbf{u}}$ and $\breve{\varphi}$ fields on $\partial\mathcal{V}_0^{\#}$. Moreover, the effective $\mathbf{u}$ and $\varphi$ fields in the RVE are set to be directly proportional to the local $\breve{\mathbf{u}}$ and $\breve{\varphi}$ of the four corner nodes, also termed as the *master* nodes. Thus, by controlling the $\breve{\mathbf{u}}$ and $\breve{\varphi}$ of the master nodes one can apply the boundary conditions in terms of the effective stress, stress and/or magnetic fields. The reader is referred to the Appendix B of (Danas, 2017) for more details on the application of the periodic boundary conditions in a coupled magneto-mechanical boundary value problem.

Once a suitable mesh and corresponding periodic boundary conditions are defined over the RVE, the local $\breve{\mathbf{u}}$ and $\breve{\varphi}$ can be computed from the augmented variational principle (35). The solution procedure initiates by constructing the local force vector and stiffness matrix for each element and followed by assembling the local stiffness matrix and applying the suitable boundary constraints (see Javili et al. (2013) for more details on the construction of the element matrices). After the local $\breve{\mathbf{u}}$ and $\breve{\varphi}$ are computed at each node for a given loading, the local fields $\breve{\mathbf{F}}$, $\breve{\mathbf{S}}$, $\breve{\boldsymbol{\sigma}}$, $\breve{\mathbf{H}}$, $\breve{\mathbf{h}}$, $\breve{\mathbf{B}}$ and $\breve{\mathbf{b}}$ are readily computed by utilizing the local kinematic and constitutive relations at the Gauss points of each element. Then, the effective mechanical and magnetic fields can be computed by direct application of (22) and (29) and volume averaging.

So far we lay out a fairly general computational framework, which is utilized to compute the effective response of an active particle-filled elastomer. Of course, the computed response depends on the specific RVE geometry, the mesh, the properties of the constituents and finally on the loading to which the RVE is subjected to. In order to assess the homogenization and the proposed phenomenological models, we compare them with the computed effective response of certain RVEs in the following section. Therein, we provide more details on the RVE geometry and the boundary and loading conditions.

## 5. Results: assessment of the theoretical models

This section provides a rigorous assessment of the proposed phenomenological models by comparison with both the analytical homogenization and the numerical finite-element (FE) estimates. The analysis is carried out in three parts. First, in Section 5.1, we assess the accuracy of the homogenization models by comparing the effective magnetization and effective magnetostriction response under zero overall mechanical pre-stress with the corresponding FE estimates. Upon this validation, in Section 5.2, we explore the accuracy of both F-H and F-B phenomenological models with the F-H homogenization model again for zero average pre-stress. Finally, in Section 5.3, we superpose mechanical pre-stressing and investigate the accuracy of the phenomenological models by comparison with the analytical homogenization model.

### *5.1. Comparison between numerical FE and analytical homogenization results*

In this section, we compare the numerical FE computations with the analytical homogenization estimates for the effective magnetization and magnetostriction response for zero mechanical pre-stress. As discussed in the previous section, we work exclusively with the F-H model for the numerical and analytical homogenization estimates. In contrast to the analytical homogenization, we carry out the numerical computations for the RVEs by considering *nearly* incompressible matrix and particle phase having both a bulk modulus $G'_{\mathtt{i}} \gg G_{\mathtt{i}}$ ($\mathtt{i} = \mathtt{m}, \mathtt{p}$). This assumption of nearly incompressible phases simplifies the FE computations considerably by avoiding the use of pressure Lagrange multipliers, which lead to additional degrees-of-freedom of the system.

Specifically, for the numerical FE computations, we consider polydisperse spherical particles comprising three different size families with a size ratio of $1 : 7/9 : 4/9$ and whose relative proportions with respect to the total particle volume are taken to be 0.6, 0.3 and 0.1, respectively (Lopez-Pamies et al., 2013; Anoukou et al., 2018). We consider three distinct particle volume fractions, $c = 0.1$, 0.2 and 0.3. In order to define the maximum particle radius, we consider a reference number of monodisperse particles, denoted with $N_{\mathtt{mono}} = 60$. Then, the radius of the maximum particle size family is simply $R_{\mathtt{max}}/L = (3c/4\pi N_{\mathtt{mono}})^{1/3}$. This readily leads to $R_{\mathtt{max}}/L = 0.074, 0.093, 0.106$ and a total number of particles $N_{\mathtt{tot}} \sim 130$, 280 and 290 for $c = 0.1$, 0.2 and 0.3, respectively. In Fig. 6, we show three such representative microstructures and the corresponding mesh, which uses standard 10-node tetrahedral quadratic elements.

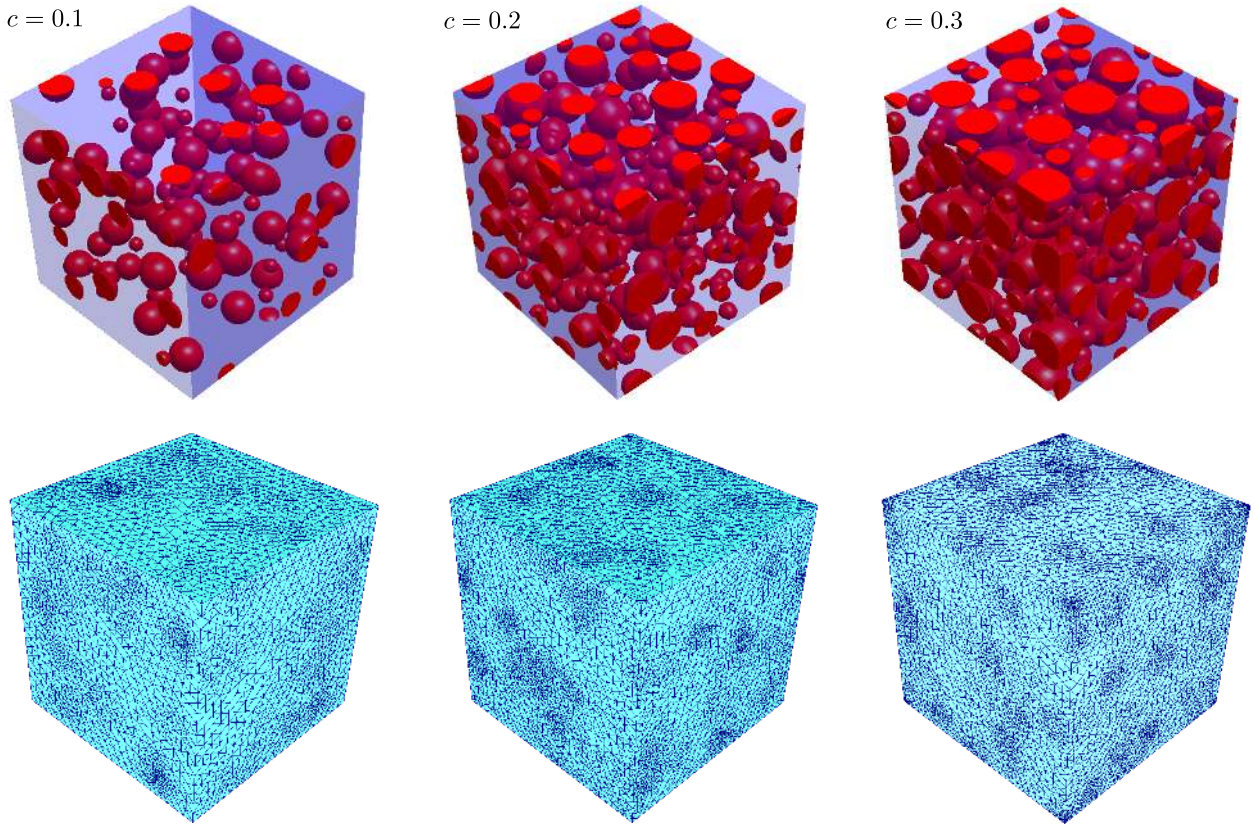


Figure 6: (top) Three representative polydisperse microstructures for $c = 0.1$, 0.2 and 0.3 having approximate number of polydisperse particles $N_{\mathtt{tot}} \sim 130$, 280 and 290, respectively. (bottom) The corresponding unstructured meshes with quadratic ten-node tetrahedral elements leading to $1.55 \times 10^6$, $1.62 \times 10^6$ and $1.50 \times 10^6$ degrees of freedom, respectively, for $c = 0.1$, 0.2 and 0.3.

In the numerical computations, we choose to work with a matrix that resembles a moderately soft silicone and thus exhibits a shear modulus in the order of 0.3MPa. The particles, in turn, are made of carbonyl iron, which exhibit a shear modulus in the order of $\sim$ 200GPa. On the other hand, the silicone matrix is magnetically inert having zero magnetic susceptibility, whereas the iron particles exhibit a Langevin saturating $m$–$h$ response. Following the recent work of Psarra et al. (2017), the initial susceptibility and saturation magnetization of the iron particles is reported in Table 2. In the following, we have chosen the material parameters as indicated in Table 2. It is noted here that use of lower shear moduli for the matrix phase leads to very large local strains, especially between two closely adjacent particles. This, in turn, leads to an extreme distortion of the mesh in those regions rendering the numerical simulations extremely difficult. Perhaps the use of a meshfree method such as the one developed by Arroyo and Ortiz (2006) and recently extended to composite-type materials Kumar et al. (2019) might allow for such computations involving very soft matrices.

Table 2: Material parameters for the silicone matrix and the carbonyl-iron particles

| | $G_{\mathtt{i}}$ (MPa) | $G'_{\mathtt{i}}/G_{\mathtt{i}}$ | $\chi_{\mathtt{i}}$ | $\mu_0 m^s_{\mathtt{i}}$ (T) | $\mu_0$ ($\mu$N·A$^2$) |
|---|---|---|---|---|---|
| Matrix ($\mathtt{i} = \mathtt{m}$) | 0.3 | 500 | 0.0 | – | $4\pi 10^{-1}$ |
| Particle ($\mathtt{i} = \mathtt{p}$) | 300 | 500 | 30.0 | 2.5 | $4\pi 10^{-1}$ |

In turn, due to the large actual contrast between the matrix and the particles, it is sufficient to consider $G_{\mathtt{p}} = 1000 G_{\mathtt{m}}$ to ensure numerical convergence as well as a sufficiently rigid response of the particles (see work of Lopez-Pamies et al. (2013)). The bulk modulus of the matrix and the particle phase are chosen to be 500 times their respective shear modulus. Such a choice for $G'$ ensures a nearly incompressible material response leading to $J \approx 1$. In order to avoid volumetric locking, the volumetric term, i.e., the term involving the $(J-1)^2$ term in (14), is under integrated by using a single Gauss point at the center of the element. The remaining of the terms in (12) are integrated using a standard 4-point Gauss quadrature for the tetrahedral elements. Finally, the effects of the two augmented terms in (35) are taken

care of by introducing a fictitious element connecting the master nodes (see details of implementation in Danas (2017)). The FE computations are carried out by developing a user-element (UEL) subroutine, which is then coupled with the commercially available finite element package ABAQUS/Standard. The developed code is rigorously benchmarked with analytical uniaxial loading solutions under both mechanical and magnetic loading. Moreover, the present comparison with the analytical homogenization estimates also serves as a benchmarking of our code.

Subsequently, we prescribe a loading path where the normal components of the average mechanical traction are equal to zero. In addition, the shear components of the deformation gradient are also blocked to ensure a uniaxial magnetostriction response. The Eulerian $h$-field $\mathbf{h}_a$ is applied in direction 1, while the response in the other directions is on average the same due to isotropy of the RVE. These boundary and loading conditions imply

$$S_{11}^{\texttt{mech}} = S_{22}^{\texttt{mech}} = S_{33}^{\texttt{mech}} = 0, \qquad F_{ij} = 0,\ \forall\ i \neq j, \qquad \mathbf{h} = \mathbf{h}_a = h\mathbf{e}_1. \tag{78}$$

The last condition is applied by constraining $|\mathbf{h}_a - \mathbf{F}^{-T}\mathbf{H}|$ to be zero via the penalty term in (35). In all the computations, the penalty parameter $\zeta$ is taken to be $10^{-3}$.

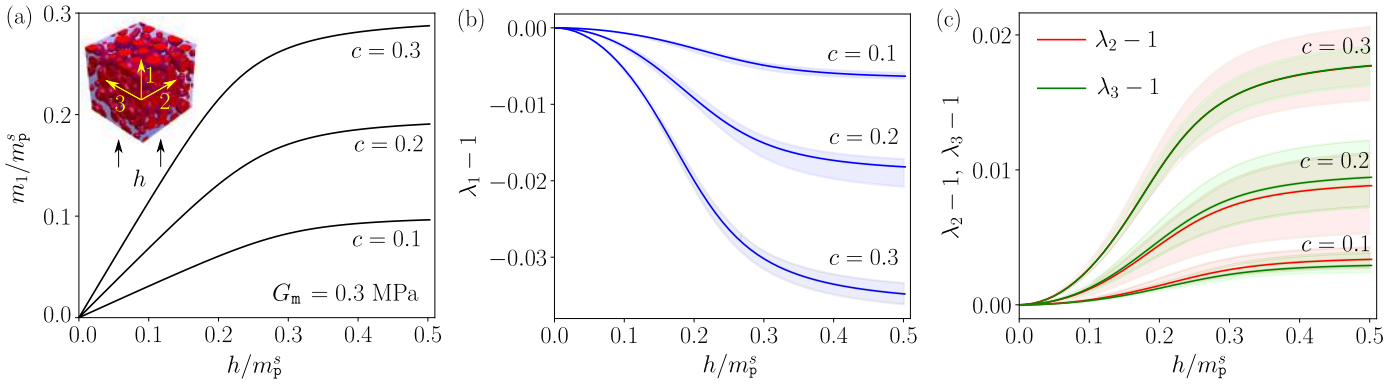


Figure 7: Numerically computed effective response of cubic RVEs comprising of random polydisperse spherical magnetizable inclusions, coming from three distinct families. The composite is subjected to an Eulerian $h$-field along the $X_1$ direction and zero overall mechanical traction. The overall Eulerian $h$-field is applied from 0 to $0.5m_{\texttt{p}}^s$ with a maximum increment of $0.01m_{\texttt{p}}^s$. (a) The effective magnetization for different particle volume fractions. Average of the (b) parallel and (c) transverse magnetostrictions (solid lines) obtained from 10 different realizations of the RVEs with $c = 0.1, 0.2$ and 0.3, along with the 95% trust regions (light patches) associated with each estimates.

First, we study the evolution of the effective magnetization and magnetostriction of a numerical RVE with the applied $h$ for volume fractions $c = 0.1, 0.2$ and 0.3. As discussed by Danas (2017) in the context of 2D RVEs, a converged magnetostriction response (i.e. in terms of scatter of the response for different realizations) necessitates an substantially large number of particles in the unit cell. The present 3D computations also show a highly fluctuating magnetostriction response in both parallel (see Fig. 7b) and transverse (see Fig. 7c) directions of the applied $h$-field. Evidently, in 3D, the computations become extremely costly by further increase of the number of particles beyond $N_{\texttt{mono}} > 60$. Therefore, we follow a second approach to obtain a converged average response. This consists in computing the effective response of the unit-cells for a sufficiently large number of realizations but a smaller number of particles (e.g., $N_{\texttt{mono}} = 60$, which leads to a total number of polydisperse particles $N_{\texttt{tot}} \sim 130$, 280 and 290 for $c = 0.1$, 0.2 and 0.3, respectively). Subsequently, by considering the average magnetostriction out of all the realizations, we assume that the response is representative in terms of a volume element. While this approach does not constitute a rigorous method to estimate the response of the RVE in a highly nonlinear setting, it still provides a useful assessment tool for the analytical solutions, even though any differences found between the numerical and the analytical homogenization model should be rationalized with extreme caution.

In this regard, we employ 10 different realizations for each volume fraction and show the average effective magnetization, parallel and transverse magnetostrictions in Fig 7a, b and c, respectively. In accord with previous studies by Danas (2017), the fluctuations in the effective magnetization $m_1$ are negligible and thus are not shown in Fig. 7a. Therein, the effective saturation magnetization $m^s$ of the composite is observed to be directly proportional to the particle volume fraction, i.e., $m^s = c\, m_{\texttt{p}}^s$. In turn, the fluctuations in the parallel magnetostriction are not negligible. The continuous lines in Fig. 7b indicate the average magnetostriction extracted from 10 realizations, whereas the light blue patches indicate the 95% trust region of the random RVE response. The trust regions of the transverse magnetostriction components are even larger (see Fig. 7c) as compared to the parallel magnetostriction one. Moreover, the transverse stretch components $\lambda_2$ and $\lambda_3$ of a unit cell may differ considerably. However, the average transverse magnetostriction components are very close indicating an acceptable convergence to isotropy (see Fig. 7c). Note that the scatter of the results observed in the average magnetostriction response is substantially larger than the one observed for the average magnetization response as well as the average purely mechanical response (not shown here but can be found in Lopez-Pamies et al. (2013)). Nonetheless, the scatter in the parallel and transverse components of the magnetostriction tend to vanish with the increase of $N_{\texttt{tot}}$. For completeness, in Appendix B, we present representative particle and mesh convergence studies for the case of $c = 0.3$ and $G_{\texttt{m}} = 0.3$ MPa.

We attempt to rationalize further the previous results by showing in Fig. 8 representative contour plots for the three volume fractions $c = 0.1$, 0.2 and 0.3 at an overall applied macroscopic field $h/m_{\texttt{p}}^s = 0.5$. The Figs. 8a-f, show the

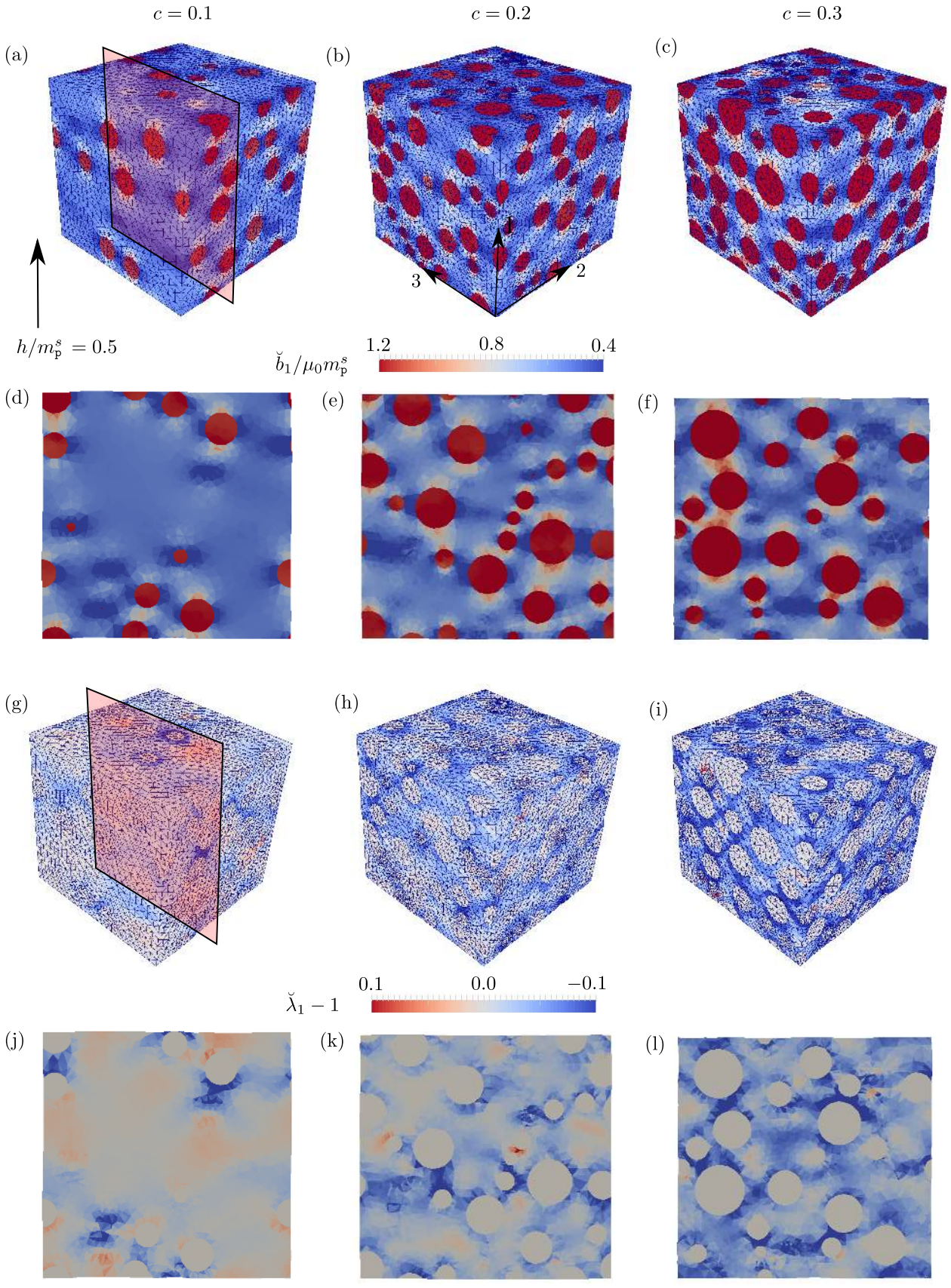


Figure 8: Numerically computed (a-c) normalized local magnetic field $\breve{b}_1/\mu_0 m_{\mathrm{p}}^s$ and (g-i) local nominal mechanical strain $\breve{\lambda}_1 - 1$ for three particle volume fractions $c = 0.1$, 0.2 and 0.3 at an overall applied macroscopic field $h/m_{\mathrm{p}}^s = 0.5$. (d-f) and (j-l) correspond to a given cross-section of the unit-cell as depicted in (a).

normalized local component $\breve{b}_1/\mu_0 m_{\mathrm{p}}^s$, whereas Figs. 8g-l, show the local nominal mechanical strain $\breve{\lambda}_1 - 1$. A first observation in the context of Figs. 8a-f is that the particle interactions exhibit a long range, which can be larger than 4 radii of the largest particle along the direction of the applied field. This interaction is stronger at higher volume fractions

(see for instance Fig. 8f), while it reveals that extreme caution needs to be taken when such material systems are analyzed with simpler dipole-dipole models. Also, the concentration of the $\breve{b}_1$ field, which can reach rather high values, is strongly dependent on local particle distributions, thus explaining partially the difficulty in obtaining a converged isotropic response under such loading conditions and magneto-mechanical loads. In other words, by slightly changing the positions of the particles, one can change substantially the corresponding interactions. In turn, Figs. 8g-l, reveal the strong concentration of strains in-between particles. These strains can reach values higher than $|0.1|$, whereas the overall straining of the RVE is $|0.03|$. Due to particle rearrangement, we also observe significant tensile strains at various points in the unit-cell. It is further noted that these strains can exceed the value of 1 when the matrix is softer, as was recently discussed by Danas (2017). Such high strains can lead to debonding and final loss of efficiency in the magneto-mechanical coupling, unless specific fabrication steps are not taken (for a more detailed discussion see Bodelot et al. (2018)). Unfortunately, in the present 3D study, we were not able to carry out such computations for softer matrices (e.g., $G_{\mathtt{m}} < 0.1$MPa) due to computational convergence problems.

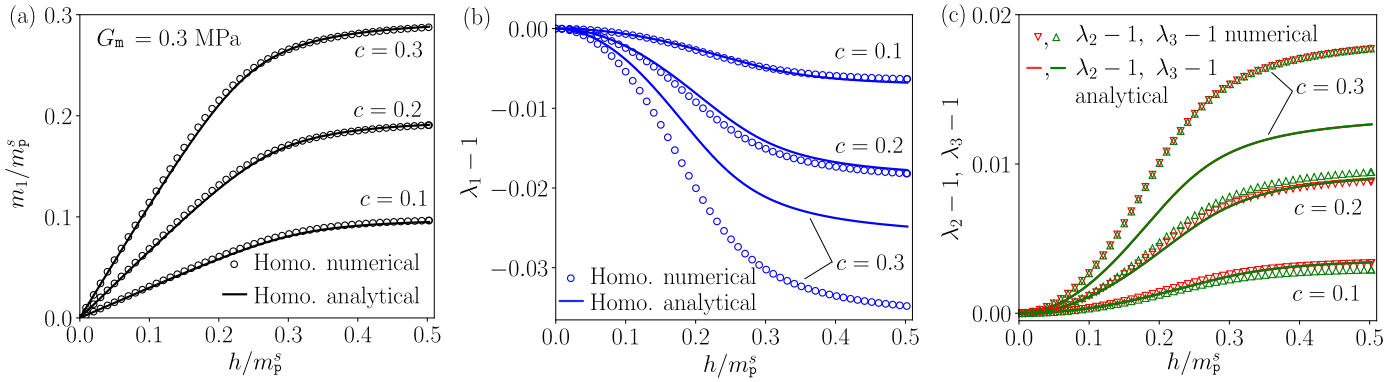


Figure 9: (a) Effective magnetization and effective (b) parallel and (c) transverse magnetostrictions as obtained from the numerical homogenization (discrete points), analytical homogenization (firm lines) for the particle volume fractions $c = 0.1, 0.2$ and 0.3. Eulerian $h$-field is applied at a local point in the MRE, which is free from mechanical tractions.

Next, we compare the average FE magnetization and magnetostriction response of Fig. 7 with those obtained from the analytical F-H homogenization model, defined in (39). Note that, the homogenization model is incompressible. Thus, we consider $\mathbf{F} = \lambda_1 \mathbf{e}_1 \otimes \mathbf{e}_1 + 1/\sqrt{\lambda_1}\mathbf{e}_2 \otimes \mathbf{e}_2 + 1/\sqrt{\lambda_1}\mathbf{e}_3 \otimes \mathbf{e}_3$ and subsequently, for a given $\mathbf{h}$, we compute $\lambda_1$ and the arbitrary pressure $p$ by solving the first two equations given by the traction conditions $(78)_1$. The magnetization and the magnetostriction response from the analytical homogenization model and the FE simulations are compared in Fig. 9. In this figure, for volume fractions $c = 0.1$ and 0.2, we observe an excellent agreement between the analytical and FE homogenization models for both the magnetization and the magnetostriction. In turn, for the higher particle volume fractions, $c = 0.3$, the analytical homogenization estimates for $\lambda_i$ $(i = 1, 2, 3)$ are significantly lower in absolute value than that obtained from the FE calculations, as shown in Figs. 9b and c. Instead, the agreement in the magnetization response is excellent even for $c = 0.3$.

In this regard, given the fact that the analytical homogenization estimates are very accurate at volume fractions of practical interest (i.e. $c \leq 0.2$), we choose them in the following to calibrate our phenomenological models even for larger volume fractions but more importantly for much lower matrix shear moduli that the FE calculations do not converge. Note, however, that the phenomenological models may be calibrated using available experimental results or directly numerical FE computations.

### *5.2. Comparison between the phenomenological and homogenization estimates without mechanical pre-load*

This section assesses the F-H (see equation (58)) and F-B (see equation (70)) incompressible phenomenological models for a large range of matrix shear moduli, spanning a range of $0.003 < G_{\mathtt{m}} < 0.3$ MPa (or equivalently $0.003 < G_{\mathtt{m}}^* < 0.3$). In particular, we choose for illustration purposes, three shear moduli $G_{\mathtt{m}} = 0.003, 0.03, 0.3$MPa. We set the magnetic properties of the iron particles, i.e., $\chi_{\mathtt{p}}$ and $m_{\mathtt{p}}^s$ unaltered (see Table 2). Finally we apply the boundary/loading conditions described in (78).

The effective magnetization and magnetostriction for $G_{\mathtt{m}}^* = 0.3, 0.03$ and 0.003 and four different volume fractions $c = 0.05, 0.1, 0.2$ and 0.3 are shown as a function of the applied Eulerian $h-$field $h/m_{\mathtt{p}}^s$ in Figs. 10a,d,g and Figs. 10b,e,h, respectively. The transverse magnetostriction components, $\lambda_2$ and $\lambda_3$, are equal to $1/\sqrt{\lambda_1}$ since we consider the MRE to be incompressible in both the analytical homogenization and the phenomenological models. We find an excellent agreement between the analytical homogenization estimates and the proposed phenomenological ones, both in terms of $m_1$ and $\lambda_1$ for all $c$ considered here.

In Figs. 10c,f,i, we show the magnetostriction $\lambda_1 - 1$ at various values of the applied Eulerian field $h/m_{\mathtt{p}}^s$. At $h = 0.2m_{\mathtt{p}}^s$, the phenomenological estimates are slightly different from the corresponding homogenization estimates for particle volume fractions $c > 0.25$. In turn, at higher $h$-fields such as $h = 0.5m_{\mathtt{p}}^s$ or $h = 1.5m_{\mathtt{p}}^s$, the phenomenological models are in very close agreement with the homogenization estimates, even for higher particle volume fractions such

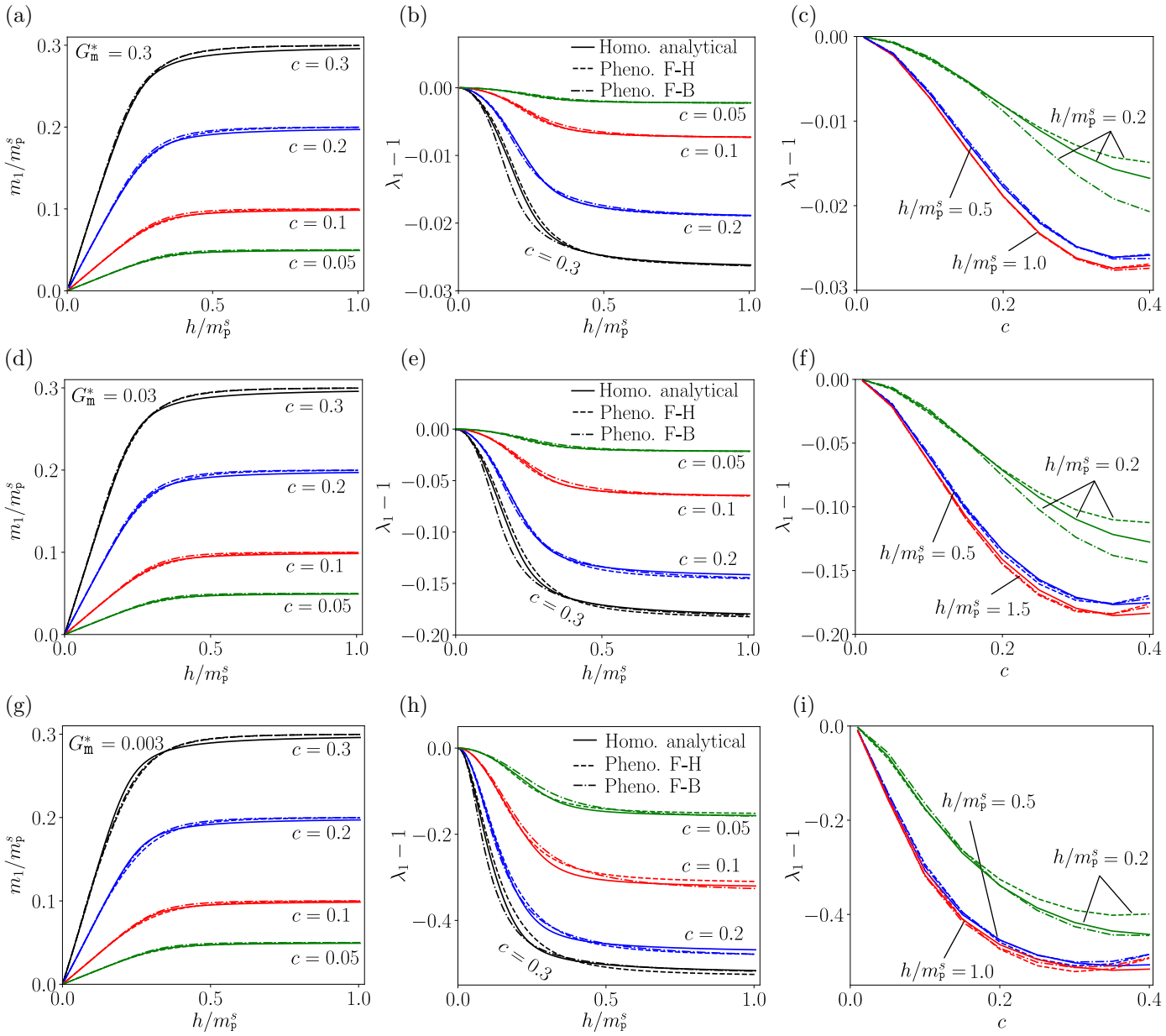


Figure 10: Effective (a,d,g) magnetization and (b,e,h) magnetostriction as a function of the applied normalized Eulerian field $h/m^s_{\mathtt{p}}$ obtained by the analytical F-H homogenization model (39) (solid lines), the phenomenological F-H model (58) (dashed lines) and the phenomenological F-B model (70) (dashed-dot lines) for particle volume fractions $c = 0.05, 0.1, 0.2$ and $0.3$ for matrix shear moduli of $G_{\mathtt{m}} = 0.3, 0.03$ and $0.003$MPa. Zero average axial mechanical pres-stress is applied. (c,f,i) Effect of particle volume fractions $c$ on the magnetostrictions at various values of $h/m^s_{\mathtt{p}}$.

as $c = 0.35$. Hence, the slight mismatch between the phenomenological and the homogenization estimates at moderate fields and large volume fraction can be directly attributed to the specific functional form of the coupling free energy (61) and (72). In turn, the calibrated coupling coefficients $\beta_2^H$ and $\beta_2^B$ manage to model very accurately the saturation magnetostriction, even for $c > 0.25$, as indicated by the almost perfect overlap of the $\lambda_1$ curves in Figs. 10c,f,i at higher applied $h$-fields. Thus, the overall performance of the phenomenological models is found to be excellent up to $c = 0.25$ and even sufficiently accurate for particle volume fraction of $c = 0.35$. We recall, here, that the homogenization estimates were found to underestimate the magnetostriction by comparison to FE results for volume fraction $c = 0.3$. Hence, the use of the proposed phenomenological models for volume fractions $c > 0.2$ should be done with caution.

Finally, an important observation in the context of Fig. 10 is that the computed magnetization response is fairly independent of the matrix shear modulus $G^*_{\mathtt{m}}$, as easily observed by comparing parts (a), (d) and (g). Instead, the magnetostriction response is a very strong function of $G^*_{\mathtt{m}}$.

### *5.3. Comparison between the phenomenological and homogenization estimates with mechanical pre-load*

The final step in the assessment of the proposed phenomenological models is to probe the model for mechanical pre-loads that lie outside the previous calibration range. We, thus, consider three different mechanical pre-loads, namely, the uniaxial pre-stress, the equibiaxial pre-stress and the pre-shear stress. In this regard, Fig. 11, 12 and 13 show the

effective magnetization and pure magnetostriction (i.e. $\lambda_1 - \lambda_1^0$ with $\lambda_1^0$ denoting the initial pre-stretching due to the applied pre-stress) for $G_{\mathtt{m}} = 0.003$ and 0.03MPa at a volume fraction $c = 0.2$ as a function of the applied Eulerian $h-$field $h/m_{\mathtt{p}}^s$. In all subsequent cases, the direction of magnetic loading is prescribed along $\mathbf{e}_1$, while the direction of applied pre-stresses are varied. The magnitude of the applied pre-stresses is selected in accord with experimentally relevant pre-stress conditions(see Danas et al. (2012)). The corresponding pre-stretches $\lambda_i^0$ $(i = 1, 2, 3)$ can be easily computed numerically or analytically for Neo-Hookean solids and are not presented explicitly here (see e.g., Danas and Triantafyllidis (2014)).

*Uniaxial pre-stress load*: The uniaxial pre-stresses are applied along the direction 1 or 2, i.e., $S_{11}^{\mathtt{mech}}/G_{\mathtt{m}} \neq 0$ or $S_{22}^{\mathtt{mech}}/G_{\mathtt{m}} \neq 0$, respectively, retaining the rest of the boundary conditions the same as those described in (78). As

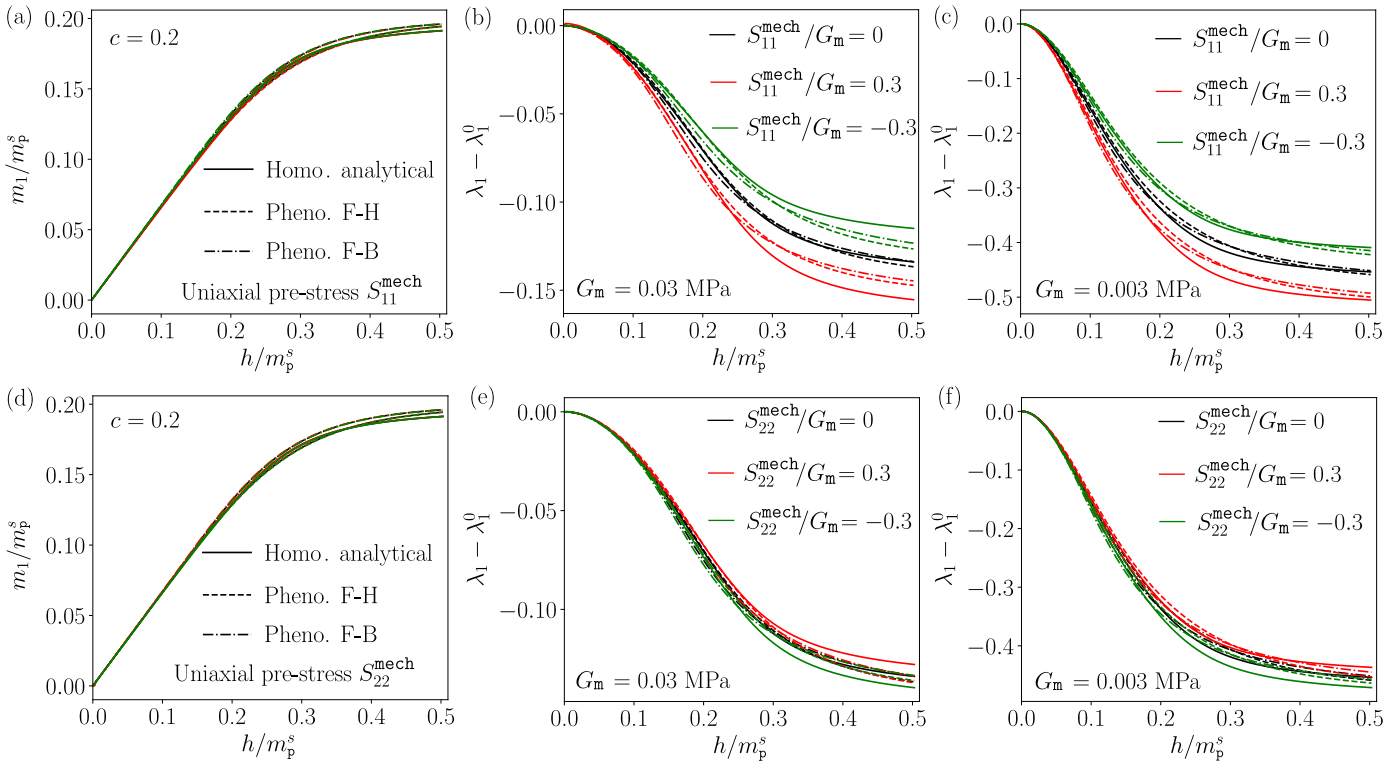


Figure 11: Effective (a,d) magnetization and (b,c,e,f) magnetostriction as a function of the applied normalized Eulerian field $h/m_{\mathtt{p}}^s$ obtained by the analytical F-H homogenization model (39) (solid lines), the phenomenological F-H model (58) (dashed lines) and the phenomenological F-B model (70) (dashed-dot lines) for particle volume fraction $c = 0.2$ and for matrix shear moduli of $G_{\mathtt{m}} = 0.03$ and 0.003MPa. (a-c) and (d-f): Two sets of average uniaxial mechanical pres-stress are applied as $S_{11}^{\mathtt{mech}}/G_{\mathtt{m}} = -0.3, 0, 0.3$ and $S_{22}^{\mathtt{mech}}/G_{\mathtt{m}} = -0.3, 0, 0.3$, respectively.

discussed before and in agreement with the earlier results of Danas et al. (2012), the magnetization response in Fig. 11a and d are independent of the matrix shear modulus $G_{\mathtt{m}}$ and the pre-stress (not labeled in the figure for clarity). All models are in excellent agreement in this case of magnetization response.

In turn, in Fig. 11b, c, e and f, the magnetostriction response depends on the pre-stress as expected. We observe that application of a tensile pre-stress $S_{11}^{\mathtt{mech}}/G_{\mathtt{m}}$ along the direction of the magnetic loading leads to an enhancement of compression, while application of a compressive pre-stress moves the magnetostriction curve upwards, i.e. to less compression. These results are in qualitative agreement with the reported experimental results in Danas et al. (2012). On the other hand, applied transverse tensile and compressive pre-stresses $S_{22}^{\mathtt{mech}}/G_{\mathtt{m}}$ leads to a reduction and an enhancement in the magnetostriction, respectively (see Fig. 11e and f). Moreover, the variability of the magnetostriction due to the transverse pre-stress $S_{22}^{\mathtt{mech}}$ is found to be weaker than the axial one, $S_{11}^{\mathtt{mech}}$.

In all these magnetostriction responses we observe that the phenomenological model, while remaining in very good agreement with the homogenization model for small to moderate values of $h$, it tends to underestimate (in absolute value) the saturating magnetostriction at higher fields. The differences between the phenomenological and homogenization estimates are larger for the higher matrix shear modulus $G_{\mathtt{m}} = 0.03$MPa, while they become much smaller for the lower one $G_{\mathtt{m}} = 0.003$MPa. Even so, the phenomenological model retains the correct characteristics even at large pre-stresses.

*Equibiaxial pre-stress load*: Equibiaxial mechanical loading together with a transverse applied magnetic field along the third direction is often encountered in layered MRE structures (Danas and Triantafyllidis, 2014; Psarra et al., 2017, 2019). Thus, motivated from such practical loading situations, we probe, next, the phenomenological model under applied equibiaxial pre-stress along directions 2 and 3, such that $S_{22}^{\mathtt{mech}}/G_{\mathtt{m}} = S_{33}^{\mathtt{mech}}/G_{\mathtt{m}} \equiv S_{\mathtt{Bi}}^{\mathtt{mech}}/G_{\mathtt{m}} \neq 0$, while the remaining boundary conditions are given by (78). Similar to the uniaxial pre-loading, no significant change in the magnetization is observed in Fig. 12a. The magnetotsriction obtained from the homogenization model is found to change in Fig. 12b and c depending on the direction of $S_{\mathtt{Bi}}^{\mathtt{mech}}/G_{\mathtt{m}}$. In turn, a very weak change is observed in the phenomenolgical magnetostriction response. We note that an equibiaxial pre-tension (pre-compression) along directions 2-3 leads to a pre-compression (pre-tension)

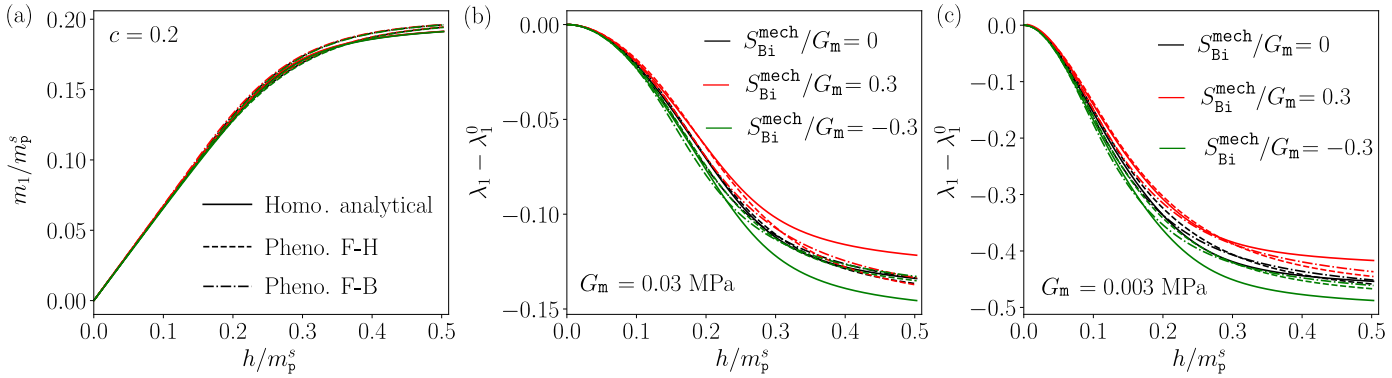


Figure 12: Effective (a) magnetization and (b,c) magnetostriction as a function of the applied normalized Eulerian field $h/m_\mathrm{p}^s$ obtained by the analytical F-H homogenization model (39) (solid lines), the phenomenological F-H model (58) (dashed lines) and the phenomenological F-B model (70) (dashed-dot lines) for particle volume fraction $c = 0.2$ and for matrix shear moduli of $G_\mathrm{m} = 0.03$ and 0.003MPa. (a-c) Three average equibiaxial mechanical pres-stress are applied, so that $S_{22}^{\mathrm{mech}}/G_\mathrm{m} = S_{33}^{\mathrm{mech}}/G_\mathrm{m} = S_{\mathrm{Bi}}^{\mathrm{mech}}/G_\mathrm{m} = -0.3, 0, 0.3$.

along 1, which is the direction of magnetic loading. Hence, the magnetostriction is observed to decrease (increase) for $S_{\mathrm{Bi}}^{\mathrm{mech}}/G_\mathrm{m} > 0$ ($S_{\mathrm{Bi}}^{\mathrm{mech}}/G_\mathrm{m} < 0$), which is in agreement with the previous observations in the context of uniaxial pre-stresses. Again the phenomenological model is in better agreement with the homogenization model at softer matrices.

*Shear pre-stress load*: The magneto-mechanical measurements in (Danas et al., 2012) also consider mechanical loading paths where a shear pre-stress is applied transverse to the applied magnetic field. Thus, a shear pre-loading is considered in this section by applying $S_{21}^{\mathrm{mech}}/G_\mathrm{m} > 0$, while keeping the rest of the boundary conditions identical to (78). In agreement with the previous observations, the magnetization remains unaffected by the applied $S_{12}^{\mathrm{mech}}$ (see Fig. 13a). In Figs. 13b

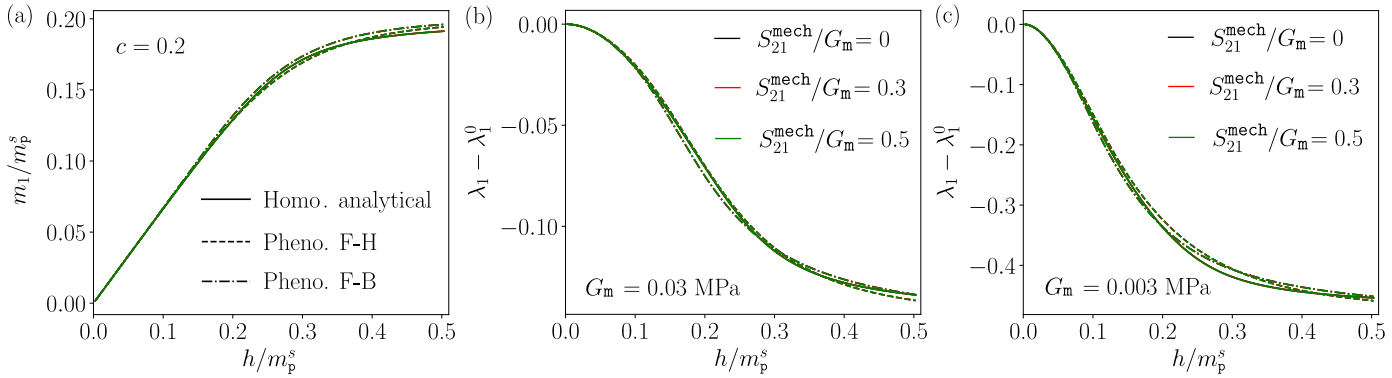


Figure 13: Effective (a) magnetization and (b,c) magnetostriction as a function of the applied normalized Eulerian field $h/m_\mathrm{p}^s$ obtained by the analytical F-H homogenization model (39) (solid lines), the phenomenological F-H model (58) (dashed lines) and the phenomenological F-B model (70) (dashed-dot lines) for particle volume fraction $c = 0.2$ and for matrix shear moduli of $G_\mathrm{m} = 0.03$ and 0.003MPa. (a-c) Three overall pre-shear stresses are applied: $S_{21}^{\mathrm{mech}}/G_\mathrm{m} = 0, 0.3, 0.5$.

and c, the magnetostriction estimates obtained by both models are *completely* independent of $S_{21}^{\mathrm{mech}}$. Furthermore, the application of $S_{21}^{\mathrm{mech}}$ leads to a shear stain and a transverse magnetization along $\mathbf{e}_2$. The resulting shear strain is interestingly found by both models to be completely independent of the applied magnetic field and thus is not included in Figs. 13b and c. Similarly, the transverse magnetization remains considerably lower ($\sim 10^{-3} m_\mathrm{p}^s$) than the parallel magnetization and thus is not included in Fig. 13a. We note in passing that very similar results are also obtained by both models for a shear pre-stress $S_{12}^{\mathrm{mech}}/G_\mathrm{m} \neq 0$ and thus is not included here for brevity.

In summary, the above results are in qualitative agreement with those in Danas et al. (2012) and suggest that MRE devices that are based on a shearing mechanical load exhibit very weak coupling along that direction and thus negligible magnetorheological stiffening. This is one of the substantial differences between MR elastomers and MR fluids, since the latter can mainly operate in shearing conditions. Instead, the MR solids can mainly operate under uniaxial and multi-axial ones.

## 6. Concluding remarks

In this work, we present explicit phenomenological models both in the $\mathbf{F} - \mathbf{H}$ and the $\mathbf{F} - \mathbf{B}$ space, which are based on a rigorous homogenization solution, which, in turn, lies in the space of the deformation gradient, $\mathbf{F}$, and Lagrangian $h-$field, $\mathbf{H}$. We analyze the magnetization and magnetostriction problem using an augmented variational principle in an effort to retrieve the pure microscopic "material" magneto-mechanical coupling in magnetorheological elastomers (MREs). We then use this framework to study numerically and analytically the homogenized response of isotropic MREs comprising $I_1-$based hyperelastic matrix and mechanically rigid iron particles that exhibit negligible

magnetic hysteresis (i.e. magnetically soft). The most important part of this study consists in proposing simple explicit homogenization-guided phenomenological models in both $\mathbf{F}-\mathbf{H}$ and $\mathbf{F}-\mathbf{B}$ variable space. Those phenomenological models are proposed both in the context of incompressible and nearly incompressible setting making them highly versatile and easy-to-implement in finite element user material subroutines.

Specifically, we show by comparison with full field FE RVE calculations that the analytical homogenization model of Lefèvre et al. (2017) is sufficiently accurate for small to moderate particle volume fractions (i.e., $0 < c \leq 0.2$). While this model is general since it is based on a rigorous homogenization procedure, it is implicit for the case of magnetically saturating particles and thus requires the solution of an additional nonlinear algebraic equation for the complete description of the MRE response. Also it is only proposed in the $\mathbf{F}-\mathbf{H}$ variable space since a Legendre-Fenchel transform is not analytically feasible in the general nonlinear magnetic saturation context. Nonetheless, it offers an extremely valuable base to investigate the response of isotropic MREs and to help calibrate phenomenological models.

In this regard, in the present study, we propose explicit phenomenological models that are based on the homogenization model. In particular, the proposed energy functions recover three main features of the Lefèvre et al. (2017) homogenization model: (i) they recover the exact (in the sense of homogenization) effective magnetization response at small and very large (i.e. at magnetization saturation) magnetic fields, (ii) they predict the exact magnetostriction response at small-to-moderate magnetic fields for any mechanical pre-loads and (iii) their purely mechanical response is exactly that of the homogenization model, which has been originally obtained in Lopez-Pamies et al. (2013). In turn, in order to maintain the simplicity of the models, we choose not to recover exactly the magnetostriction response at very large saturating magnetic fields (but see along these directions the recent work in the $\mathbf{F}-\mathbf{H}$ space of Lefèvre et al. (2019)). In particular, in a number of applications that the geometry plays a predominant role (see for instance Psarra et al. (2019)) or the coupling is weak (i.e., at fairly large shear moduli of the matrix phase, e.g. larger than 0.3MPa for instance), the coupled part of the energy can be easily dropped while maintaining the dependence on the volume fraction of the particles in the mechanical and magnetic energy. This last modeling approach is straightforward and fairly accurate for such applications and requires a minimum set of calibration such as the mechanical and purely magnetic constitutive parameters of the MRE.

Specifically, in order to obtain the nontrivial behavior of the magnetostrictive response as a function of the applied Eulerian magnetic field (i.e., is initially quadratic, subsequently increases in a slower non-quadratic manner reaching a saturating value), we propose a coupling energy that is a nonconvex function of its argument. It is noted, however, that the coefficient multiplying this coupling part is rather small thus leading to an overall convex magneto-elastic energy function. Even so, it is evident from that observation that for more complex MREs (i.e. with non-spherical particles or particle-chain distributions) such nonconvexities could lead to instabilities and loss of ellipticity (see for instance Otténio et al. (2007), Danas and Triantafyllidis (2014) and Psarra et al. (2017, 2019)). Such an analysis is beyond the scope of the present manuscript and is left for a future study.

Furthermore, the proposed phenomenological model comprises very few calibration parameters, which in the present study are reduced to a single one, i.e., $\beta_2^{H,\tilde{B}}$. This parameter is then calibrated numerically by comparison with the analytical homogenization model of Lefèvre et al. (2017). Nevertheless, the form of the phenomenological energy functions is more universal and can be used more generally in fitting any experimental or numerical estimates that may be available. As also been shown, extrapolation of the phenomenological estimates in a regime that lies rather far from the calibration process (e.g. significant applied pre-stresses) gives very satisfactory and accurate results at small and moderate applied magnetic fields and even large fields particularly for softer matrices.

By using the simple explicit energy functions together with the variational framework of Danas (2017) that allows to study the pure material magneto-mechanical coupling, we have obtained several interesting results. SPecifically, all presented models show that in the context of isotropic MREs, the magnetization response is insensitive to the shear modulus of the matrix material even when the latter ranges from values between 0.003-0.3MPa (this observation is also valid for the larger range 0.001-1MPa not explicitly shown here). On the other hand, the magnetostriction response is highly dependent of the shear modulus of the matrix $G_{\mathtt{m}}$, as intuitively expected. A second observation, which is consistent with the recent work of Danas (2017), is that the microscopic deformation of isotropic MREs leads to compressive magnetostriction for zero overall mechanical tractions in the RVE. Hence, the observed overall extensive response of MRE specimens in experiments (see for instance Bodelot et al. (2018)) is a result of the specimen shape and the entire set of boundary conditions and geometry of the experimental setup. This has been discussed in detail in Lefèvre et al. (2017), who showed that in zones of (almost) zero mechanical tractions, the MRE exhibits compressive strains. Finally, application of pre-stresses results in the phenomenological models becoming less accurate especially at larger magnetic fields, even though their predictions become increasingly better for softer matrices. Finally, we find that the effect of a mechanical pre-load is maximum for uniaxial pre-stressing and negligible for shearing ones.

In closing, it is worth mentioning that the actual MREs may be viscoelastic in nature and thus the extension of the present work to that context is necessary. Recent studies towards that direction revealed several interesting features (see for instance Saxena et al. (2013) and Sánchez et al. (2018)), however, no constitutive micromechanical models that take into account the particle volume fraction and microstructure have been proposed yet. Furthermore, in even more recent works, the iron particles have been replaced by hard magnetic particles such as NdFeB-particles adding one more level of complexity, that of magnetic hysteresis (see recent work of Mukherjee and Danas (2019)). Such a study that builds upon the present one is underway.

**Acknowledgments**

The authors would like to thank Prof. Victor Lefèvre and Prof. Oscar Lopez-Pamies for many useful discussions and valuable suggestions. Support from the European Research Council (ERC) under the European Union's Horizon 2020 research and innovation program (grant agreement No 636903 - MAGNETO) is highly acknowledged. The computational part of this work was supported by the ANR under contract number ANR-10-EQPX-37.

## Appendix A: Pull-back transformation of effective Eulerian field h

The effective Eulerian $h$-field is defined by (24), such that

$$\mathbf{h} = \frac{1}{\mathcal{V}^{\#}} \int_{\mathcal{V}^{\#}} \breve{\mathbf{h}}(\mathbf{x}) \, \mathrm{d}v. \tag{A.1}$$

Substituting $\breve{\mathbf{h}}(\mathbf{x})$ by its pull-back transformation $(2)_2$ and expressing the current volume $\mathcal{V}^{\#} = J\mathcal{V}_0^{\#}$ in the above, we obtain

$$\mathbf{h} = \frac{1}{J\mathcal{V}_0^{\#}} \int_{\mathcal{V}_0^{\#}} \breve{J}(\mathbf{X}) \breve{\mathbf{F}}^{-T}(\mathbf{X}) \cdot \breve{\mathbf{H}}(\mathbf{X}) \, \mathrm{d}V = \frac{1}{J\mathcal{V}_0^{\#}} \int_{\mathcal{V}_0^{\#}} \frac{\partial \breve{J}}{\partial \breve{\mathbf{F}}}(\mathbf{X}) \cdot \breve{\mathbf{H}}(\mathbf{X}) \, \mathrm{d}V, \tag{A.2}$$

where the microscopic deformation gradient $\breve{\mathbf{F}}$ is defined in Section 2 via $\breve{\mathbf{F}}(\mathbf{X}) = \mathrm{Grad}\ \mathbf{y}(\mathbf{X})$, with $\mathbf{y}(\mathbf{X})$ denoting the continuous and twice differentiable one-to-one mapping from the reference to the current configuration. The deformation gradient tensor $\breve{\mathbf{F}}$ can then be expressed in index notation as $\breve{F}_{mn} = \mathrm{y}_{m,n}$, where the comma "," in the subscript denotes partial differentiation with respect to $\mathbf{X}$, such that $\mathrm{y}_{m,n} = \partial \mathrm{y}_m / \partial X_n$. Furthermore, $\breve{J} = \det \breve{\mathbf{F}}$ in (A.2) can be expressed in index notation as

$$\breve{J} = \frac{1}{6} \epsilon_{ijk} \epsilon_{pqr} \mathrm{y}_{i,p} \mathrm{y}_{j,q} \mathrm{y}_{k,r}, \tag{A.3}$$

where $\epsilon_{ijk}$ is the standard permutation symbol.

To obtain the pull-back transformation of $\mathbf{h}$ in terms of $\mathbf{F}$ and $\mathbf{H}$ in the average context, we first show that the tensor $\partial \breve{J} / \partial \breve{\mathbf{F}}$ is divergence-free and then utilize this condition along with the kinematically admissible boundary conditions on $\breve{\mathbf{H}}$ or $\partial \breve{J} / \partial \breve{\mathbf{F}}$ and the Hill-Mandel lemma.

*Divergence of* $\partial \breve{J} / \partial \breve{\mathbf{F}}$: The tensor $\partial \breve{J} / \partial \breve{\mathbf{F}}$ is readily evaluated from (A.3), such that

$$\frac{\partial \breve{J}}{\partial \breve{F}_{mn}} = \frac{1}{2} \left[ \epsilon_{mjk} \epsilon_{nqr} \mathrm{y}_{j,q} \mathrm{y}_{k,r} \right]. \tag{A.4}$$

In turn, $\mathrm{Div}(\partial \breve{J} / \partial \breve{\mathbf{F}})$ can be computed by taking the divergence on both sides of the above equation, such that

$$\left( \frac{\partial \breve{J}}{\partial \breve{F}_{mn}} \right)_{,n} = \frac{1}{2} \left[ \epsilon_{mjk} \epsilon_{nqr} \mathrm{y}_{j,qn} \mathrm{y}_{k,r} + \epsilon_{mjk} \epsilon_{nqr} \mathrm{y}_{j,q} \mathrm{y}_{k,rn} \right].$$

By interchanging the dummy indices in the previous equation, one gets the desired divergence-free result

$$\left( \frac{\partial \breve{J}}{\partial \breve{F}_{mn}} \right)_{,n} = \frac{1}{2} \epsilon_{mjk} \mathrm{y}_{j,q} \left[ \epsilon_{nqr} \mathrm{y}_{k,rn} - \epsilon_{nqr} \mathrm{y}_{k,nr} \right] = 0. \tag{A.5}$$

*Application of the Hill-Mandel lemma*: We express (A.2) in index notation as

$$h_i = \frac{1}{J\mathcal{V}_0^{\#}} \int_{\mathcal{V}_0^{\#}} \frac{\partial \breve{J}}{\partial \breve{F}_{ij}} \breve{H}_j \, \mathrm{d}V = -\frac{1}{J\mathcal{V}_0^{\#}} \int_{\mathcal{V}_0^{\#}} \frac{\partial \breve{J}}{\partial \breve{F}_{ij}} \breve{\varphi}_{,j} \, \mathrm{d}V. \tag{A.6}$$

Here, the curl-free condition on $\breve{\mathbf{H}}$ allows to write the latter in terms of a scalar potential $\breve{\varphi}$ such that $\breve{\mathbf{H}} = -\mathrm{Grad} \breve{\varphi}$ (or equivalently, $\breve{H}_i = -\breve{\varphi}_{,i}$). From the divergence theorem and the divergence-free property of $\partial \breve{J} / \partial \breve{\mathbf{F}}$, we recast (A.6) to read

$$h_i = -\frac{1}{J\mathcal{V}_0^{\#}} \int_{\partial \mathcal{V}_0^{\#}} \frac{\partial \breve{J}}{\partial \breve{F}_{ij}} \breve{\varphi} \mathcal{N}_j \, \mathrm{d}S, \tag{A.7}$$

where $\mathcal{N}_j$ is the unit normal on the reference boundary $\partial \mathcal{V}_0^{\#}$. Notice that, in $\mathcal{V}_0^{\#}$, the scalar potential $\breve{\varphi}$ is defined by $(23)_2$ to be $\breve{\varphi} = -H_k X_k + \widetilde{\varphi}$ with $\widetilde{\varphi}$ periodic (i.e. takes identical values in opposite faces of the periodic boundary). Next, substituting this last expression in (A.7), we obtain

$$h_i = \frac{1}{J\mathcal{V}_0^{\#}} \left\{ \int_{\partial \mathcal{V}_0^{\#}} \frac{\partial \breve{J}}{\partial \breve{F}_{ij}} H_k X_k \mathcal{N}_j \, \mathrm{d}S - \int_{\partial \mathcal{V}_0^{\#}} \widetilde{\varphi} \frac{\partial \breve{J}}{\partial \breve{F}_{ij}} \mathcal{N}_j \, \mathrm{d}S \right\}, \tag{A.8}$$

where we recall that the effective $H_k$ is constant. The second term in (A.8) is identically zero since $\widetilde{\varphi}$ is periodic and the term $\mathcal{N}_j \partial \breve{J}/\partial \breve{F}_{ij}$ is anti-periodic (by simple use of the divergence-free property of $\partial \breve{J}/\partial \breve{F}_{ij}$). In turn, by employing the divergence theorem in the first term of (A.8) together with the divergence-free property of $\partial \breve{J}/\partial \breve{F}_{ij}$, we obtain

$$h_i = \frac{1}{J\mathcal{V}_0^{\#}} \int_{\mathcal{V}_0^{\#}} \frac{\partial \breve{J}}{\partial \breve{F}_{ij}} H_k \delta_{kj} \, \mathrm{d}V = \frac{1}{J} \left[ \frac{1}{\mathcal{V}_0^{\#}} \int_{\mathcal{V}_0^{\#}} \frac{\partial \breve{J}}{\partial \breve{F}_{ij}} \, \mathrm{d}V \right] H_j. \tag{A.9}$$

Again, using the divergence-free property of $\partial \breve{J}/\partial \breve{F}_{ij}$, the last term in the square brackets is simply equal to the average $\partial J/\partial F_{ij}$, such that

$$h_i = \frac{1}{J} \frac{\partial J}{\partial F_{ij}} H_j = F_{ji}^{-1} H_j, \qquad \text{or} \qquad \mathbf{h} = \mathbf{F}^{-T} \cdot \mathbf{H}. \tag{A.10}$$

## Appendix B: Particle and mesh convergence

This section presents a convergence study of the computed effective magnetization and magnetostriction for a particle volume fraction $c = 0.3$ in terms of the overall number of particles in the RVE and the number of degrees of freedom. It has been observed in Section 5.1 as well as in former numerical homogenization estimates (Danas, 2017) that the effective magnetization exhibits negligible scatter when different realizations of RVEs are considered. We thus exclude for brevity the convergence study in terms of the effective magnetization and focus only on the magnetostriction results.

For all the computations performed hereafter, the material parameters for the particle and the matrix phases are those presented in Table 2. Moreover, the applied overall (macroscopic) boundary conditions remain the same with those described in equation (78).

*Convergence of the number of particles*: In addition to a set of 10 realizations of the polydisperse RVEs having $N_{\mathtt{mono}} = 60$ ($N_{\mathtt{tot}} \sim 290$) considered in Section 5.1, we analyze here two additional sets of 10 RVEs each. As defined in Section 5.1, in the first set of RVEs, we use the same three different families having the same size ratio (i.e. $(1, 7/9, 4/9)$) and relative volume proportion $(0.6, 0.3, 0.1)c$, respectively. Furthermore, it comprises polydisperse spherical particles obtained by setting $N_{\mathtt{mono}} = 100$, which leads to a $R_{\mathtt{max}}/L = 0.0895$ (with $L = 1$ denoting the size of the cubic unit cell) and a total number of actual particles $N_{\mathtt{tot}} \sim 450$. The last set has 10 RVE realizations with polydisperse spherical particles from four different families of size ratio 1.0, 0.778, 0.556, and 0.333 whose relative proportion in the total particle volume being 0.6, 0.3, 0.2 and 0.1, respectively. This last set is obtained by considering $N_{\mathtt{mono}} = 120$, which leads to a maximum sphere radius $R_{\mathtt{max}}/L = 0.0842$ and a total number of particles $N_{\mathtt{tot}} \sim 750$. The average value of the total degrees of freedom for each set of RVEs is $1.5 \times 10^6$, $2.7 \times 10^6$ and $8.5 \times 10^5$ for $N_{\mathtt{tot}} \sim 290$, 450 and 750, respectively. Notice that, the $N_{\mathtt{tot}}$ in these polydisperse RVEs is not a primary variable, rather, is a derived quantity. The primary variables that define a polydisperse RVE is given by the particle volume fraction $c$, the equivalent number of monodisperse particles $N_{\mathtt{mono}}$, the size ratio of different families and their relative volume proportions. For a detailed discussion of these RVE constructions the reader is referred to the recent works of Anoukou et al. (2018), Zerhouni et al. (2019) and Tarantino et al. (2019).

The average of the computed magnetostriction responses for the three aforementioned sets of RVEs are shown in Fig B.1a. Here we observe that, with increasing number of particles, the average parallel $(\lambda_1 - 1)$ and transverse $(\lambda_2 - 1,\ \lambda_3 - 1)$ magnetostrictions converge to that reported in Fig 7b and c, respectively. Furthermore, the scatter of the computed magnetostrictions are observed to decrease considerably (see Fig. B.1b) with the increase of the number of particles. It should be noted here that the convergence of the computed magnetostriction in Fig. B.1a and b is valid for

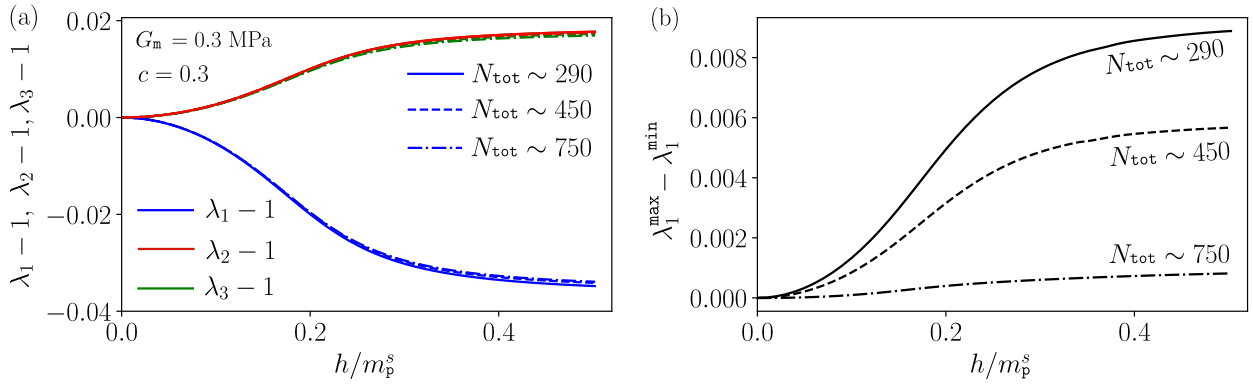


Figure B.1: (a) Average effective parallel and transverse magnetostriction stretches, (b) scatter in the parallel magnetostrictions as obtained from the numerical homogenization for the particle volume fraction of $c = 0.3$ and the total number of particles $N_{\mathtt{tot}} \sim 290$ (firm lines), $N_{\mathtt{tot}} \sim 450$ (dashed lines) and $N_{\mathtt{tot}} \sim 750$ (chain-dotted lines). Eulerian $h$-field is applied at a local point in the MRE, which is free from mechanical tractions.

the present use of energy functions (e.g. Neo-Hookean mechanical response defined in (14)). A different hyperelastic law

with more pronounced nonlinearities (such as Gent hyperelasticity) for the matrix phase may need additional convergence studies and perhaps even larger number of particles.

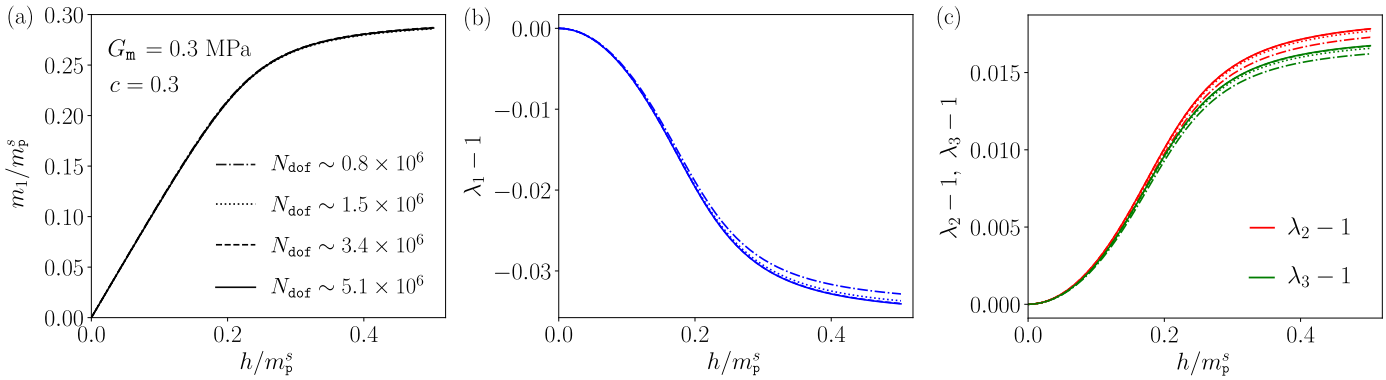


Figure B.2: Computed (a) effective magnetization and (b-c) effective parallel and transverse magnetostrictions for a RVE with $c = 0.3$ and $N_{\mathrm{tot}} \sim 290$ having four different meshes with total degrees-of-freedom $0.8 \times 10^6$ (dashed-dotted lines), $1.5 \times 10^6$ (dotted lines), $3.4 \times 10^6$ (dashed lines) and $5.1 \times 10^6$ (solid lines).

*Mesh convergence*: Next, we investigate the mesh convergence of the computed effective magnetization and magnetostriction for a specific RVE given by Fig. 7 for $c = 0.3$. In addition to the given mesh in Fig. 7, we perform the computations for three additional meshes; one with a coarser mesh with total number of degrees of freedom equal to $0.8 \times 10^6$ and two with finer meshes having $3.4 \times 10^6$ and $5.1 \times 10^6$ degrees of freedom. As shown in Fig. B.2a, the effective magnetization is converging rapidly for all meshes, whereas, the parallel and transverse magnetostrictions in Fig. B.2b and c are seen to be slightly underestimated when the coarse mesh with $0.8 \times 10^6$ degrees-of-freedom is used. Nevertheless, the magnetostriction response is observed to converge rapidly with the subsequent mesh refinements. Notice that in all the reported results in Section 5.1, we use the RVEs with approximately $1.5 \times 10^6$ degrees of freedom, which leads to fully converged magnetization and magnetostriction responses as observed in Fig. B.2.

## References


Abramowitz, M., Stegun, I., 1972. Handbook of Mathematical Functions. Dover, New York.

Anoukou, K., Brenner, R., Hong, F., Pellerin, M., Danas, K., 2018. Random distribution of polydisperse ellipsoidal inclusions and homogenization estimates for porous elastic materials. Comp. Struct. 210, 87 – 101.
URL http://www.sciencedirect.com/science/article/pii/S0045794918304565

Arroyo, M., Ortiz, M., 2006. Local maximum-entropy approximation schemes: a seamless bridge between finite elements and meshfree methods. International Journal for Numerical Methods in Engineering 65 (13), 2167–2202.
URL https://onlinelibrary.wiley.com/doi/abs/10.1002/nme.1534

Bodelot, L., Pössinger, T., Danas, K., Triantafyllidis, N., Bolzmacher, C., 2016. Magnetorheological elastomers: Experimental and modeling aspects. In: Ralph, C., Silberstein, M., Thakre, P. R., Singh, R. (Eds.), Mechanics of Composite and Multi-functional Materials, Volume 7. Springer International Publishing, Cham, pp. 251–256.

Bodelot, L., Voropaieff, J.-P., Pössinger, T., 2018. Experimental investigation of the coupled magneto-mechanical response in magnetorheological elastomers. Exp Mech 58 (2), 207–221.
URL https://doi.org/10.1007/s11340-017-0334-7

Bustamante, R., 2010. Transversely isotropic nonlinear magneto-active elastomers. Acta Mechanica 210 (3-4), 183–214.
URL https://doi.org/10.1007/s00707-009-0193-0

Bustamante, R., Dorfmann, A., Ogden, R., 2008. On variational formulations in nonlinear magnetoelastostatics. Mathematics and Mechanics of Solids 13 (8), 725–745.
URL https://doi.org/10.1177/1081286507079832

Bustamante, R., Dorfmann, A., Ogden, R., 2011. Numerical solution of finite geometry boundary-value problems in nonlinear magnetoelasticity. International Journal of Solids and Structures 48 (6), 874 – 883.
URL http://www.sciencedirect.com/science/article/pii/S0020768310004208

Bustamante, R., Ogden, R. W., 2012. Nonlinear magnetoelastostatics: Energy functionals and their second variations. Mathematics and Mechanics of Solids 18 (7), 760–772.
URL https://doi.org/10.1177/1081286512448347

Danas, K., 2017. Effective response of classical, auxetic and chiral magnetoelastic materials by use of a new variational principle. J. Mech. Phys. Solids 105, 25–53.

Danas, K., Kankanala, S., Triantafyllidis, N., 2012. Experiments and modeling of iron-particle-filled magnetorheological elastomers. J. Mech. Phys. Solids 60 (1), 120–138.
URL http://www.sciencedirect.com/science/article/pii/S0022509611001736

Danas, K., Triantafyllidis, N., 2014. Instability of a magnetoelastic layer resting on a non-magnetic substrate. J. Mech. Phys. Solids 69, 67 – 83.

Diguet, G., Beaugnon, E., Cavaillé, J., 2010. Shape effect in the magnetostriction of ferromagnetic composite. J. Magn. Magn. Mater. 322 (21), 3337 – 3341.
URL http://www.sciencedirect.com/science/article/B6TJJ-5093N8V-2/2/d5878c0abd20adc88cdb94281950f912

Dorfmann, A., Ogden, R., 2004. Nonlinear magnetoelastic deformations of elastomers. Acta Mechanica 167 (1-2), 13–28.
URL https://doi.org/10.1007/s00707-003-0061-2

Dorfmann, A., Ogden, R. W., 2005. Some problems in nonlinear magnetoelasticity. Zeitschrift für angewandte Mathematik und Physik ZAMP 56 (4), 718–745.
URL http://dx.doi.org/10.1007/s00033-004-4066-z

Galipeau, E., Ponte Castañeda, P., 2013. A finite-strain constitutive model for magnetorheological elastomers: Magnetic torques and fiber rotations. J Mech Phys Solids 61 (4), 1065–1090.
URL http://www.sciencedirect.com/science/article/pii/S0022509612002463

Galipeau, E., Rudykh, S., deBotton, G., Ponte Castañeda, P., 2014. Magnetoactive elastomers with periodic and random microstructures. International Journal of Solids and Structures 51 (18), 3012 – 3024.
URL http://www.sciencedirect.com/science/article/pii/S0020768314001681

Ginder, J., Nichols, M., Elie, L., Tardiff, J., 1999. Magnetorheological elastomers: properties and applications. Smart Mater Struct 3675, 131–138.

Hankin, R. K., 2015. Numerical evaluation of the gauss hypergeometric function with the hypergeo package. The R Journal 7, 81–88.

Henann, D. L., Chester, S. A., Bertoldi, K., 2013. Modeling of dielectric elastomers: Design of actuators and energy harvesting devices. J Mech Phys Solids 61 (10), 2047 – 2066.
URL http://www.sciencedirect.com/science/article/pii/S0022509613000926

Javili, A., Chatzigeorgiou, G., Steinmann, P., 2013. Computational homogenization in magneto-mechanics. International Journal of Solids and Structures 50 (25-26), 4197–4216.
URL https://doi.org/10.1016/j.ijsolstr.2013.08.024

Jolly, M. R., Carlson, J. D., Muñoz, B. C., Bullions, T. A., 1996. The magnetoviscoelastic response of elastomer composites consisting of ferrous particles embedded in a polymer matrix. Journal of Intelligent Material Systems and Structures 7 (6), 613–622.
URL https://doi.org/10.1177/1045389X9600700601

Kalina, K. A., Metsch, P., Kästner, M., 2016. Microscale modeling and simulation of magnetorheological elastomers at finite strains: A study on the influence of mechanical preloads. International Journal of Solids and Structures 102-103, 286 – 296.
URL http://www.sciencedirect.com/science/article/pii/S0020768316303109

Kankanala, S. V., Triantafyllidis, N., 2004. On finitely strained magnetorheological elastomers. J. Mech. Phys. Solids 52 (12), 2869 – 2908.
URL http://www.sciencedirect.com/science/article/B6TXB-4D5P2GW-1/2/54fb91d5b0a08991f9819e91ab1690b2

Keip, M.-A., Rambausek, M., 2015. A multiscale approach to the computational characterization of magnetorheological elastomers. Int J Numer Methods Eng 7, 23–32, nme.5178.
URL http://dx.doi.org/10.1002/nme.5178

Keip, M.-A., Sridhar, A., nov 2018. A variationally consistent phase-field approach for micro-magnetic domain evolution at finite deformations. Journal of the Mechanics and Physics of Solids.
URL https://doi.org/10.1016/j.jmps.2018.11.012

Kim, Y., Yuk, H., Zhao, R., Chester, S. A., Zhao, X., Jun 2018. Printing ferromagnetic domains for untethered fast-transforming soft materials. Nature 558 (7709), 274–279.
URL http://dx.doi.org/10.1038/s41586-018-0185-0

Kumar, S., Danas, K., Kochmann, D. M., 2019. Enhanced local maximum-entropy approximation for stable meshfree simulations. Computer Methods in Applied Mechanics and Engineering 344, 858 – 886.
URL http://www.sciencedirect.com/science/article/pii/S0045782518305346

Landis, C. M., 2002. A new finite-element formulation for electromechanical boundary value problems. International Journal for Numerical Methods in Engineering 55 (5), 613–628.
URL http://dx.doi.org/10.1002/nme.518

Lefèvre, V., Danas, K., Lopez-Pamies, O., 2017. A general result for the magnetoelastic response of isotropic suspensions of iron and ferrofluid particles in rubber, with applications to spherical and cylindrical specimens. J. Mech. Phys. Solids 107, 343–364.

Lefèvre, V., Danas, K., Lopez-Pamies, O., 2019. Two families of explicit models constructed from a homogenization solution for the magnetoelastic response of mres containing iron and ferrofluid particles. International Journal of Non-Linear Mechanics.
URL http://www.sciencedirect.com/science/article/pii/S0020746219306237

Lefèvre, V., Lopez-Pamies, O., 2016a. Nonlinear electroelastic deformations of dielectric elastomer composites: I — ideal elastic dielectrics. J Mech Phys Solids 99, 409–437.
URL http://www.sciencedirect.com/science/article/pii/S0022509616301478

Lefèvre, V., Lopez-Pamies, O., 2016b. Nonlinear electroelastic deformations of dielectric elastomer composites: II — non-gaussian elastic dielectrics. J Mech Phys Solids 99, 438–470.
URL http://www.sciencedirect.com/science/article/pii/S002250961630148X

Liu, L., James, R., Leo, P., 2006. Magnetostrictive composites in the dilute limit. J. Mech. Phys. Solids 54 (5), 951 – 974.
URL http://www.sciencedirect.com/science/article/B6TXB-4J0NYDR-1/2/b7d873348c33983b6b53186b9aca876d

Lopez-Pamies, O., 2014. Elastic dielectric composites: Theory and application to particle-filled ideal dielectrics. Journal of the Mechanics and Physics of Solids 64, 61–82.
URL https://doi.org/10.1016/j.jmps.2013.10.016

Lopez-Pamies, O., Goudarzi, T., Danas, K., 2013. The nonlinear elastic response of suspensions of rigid inclusions in rubber: II - a simple explicit approximation for finite-concentration suspensions. J Mech Phys Solids 61 (1), 19 – 37.
URL http://www.sciencedirect.com/science/article/pii/S0022509612001925

Martin, J. E., Anderson, R. A., Read, D., Gulley, G., Nov 2006. Magnetostriction of field-structured magnetoelastomers. Phys. Rev. E 74, 051507.
URL http://link.aps.org/doi/10.1103/PhysRevE.74.051507

Metsch, P., Kalina, K. A., Spieler, C., Kästner, M., 2016. A numerical study on magnetostrictive phenomena in magnetorheological elastomers. Computational Materials Science 124, 364 – 374.
URL http://www.sciencedirect.com/science/article/pii/S0927025616303822

Miehe, C., Vallicotti, D., Teichtmeister, S., 2016. Homogenization and multiscale stability analysis in finite magneto-electro-elasticity. application to soft matter ee, {ME} and {MEE} composites. Comput Methods Appl Mech Eng 300, 294 – 346.
URL http://www.sciencedirect.com/science/article/pii/S0045782515003321

Mukherjee, D., Danas, K., 2019. An evolving switching surface model for ferromagnetic hysteresis. Journal of Applied Physics 125 (3), 033902.
URL https://doi.org/10.1063/1.5051483

Otténio, M., Destrade, M., Ogden, R. W., Sep 2007. Incremental magnetoelastic deformations, with application to surface instability. Journal of Elasticity 90 (1), 19–42.
URL http://dx.doi.org/10.1007/s10659-007-9120-6

Perger, W. F., Bhalla, A., Nardin, M., 1993. A numerical evaluator for the generalized hypergeometric series. Computer physics communications 77 (2), 249–254.

Ponte Castañeda, P., Galipeau, E., 2011. Homogenization-based constitutive models for magnetorheological elastomers at finite strain. Journal of the Mechanics and Physics of Solids 59 (2), 194–215.
URL https://doi.org/10.1016/j.jmps.2010.11.004

Psarra, E., Bodelot, L., Danas, K., 2017. Two-field surface pattern control via marginally stable magnetorheological elastomers. Soft Matter 13, 6576–6584.

URL http://dx.doi.org/10.1039/C7SM00996H
Psarra, E., Bodelot, L., Danas, K., 2019. Wrinkling to crinkling transitions and curvature localization in a magnetoelastic film bonded to a non-magnetic substrate. Journal of the Mechanics and Physics of Solids 133, 103734.
URL https://doi.org/10.1016/j.jmps.2019.103734
Rintoul, M. D., Torquato, S., 1997. Reconstruction of the structure of dispersions. Journal of Colloid and Interface Science 186 (2), 467–476.
URL https://doi.org/10.1006/jcis.1996.4675
Sánchez, P. A., Gundermann, T., Dobroserdova, A., Kantorovich, S. S., Odenbach, S., 2018. Importance of matrix inelastic deformations in the initial response of magnetic elastomers. Soft Matter.
URL https://doi.org/10.1039/c7sm02366a
Saxena, P., Hossain, M., Steinmann, P., 2013. A theory of finite deformation magneto-viscoelasticity. International Journal of Solids and Structures 50 (24), 3886 – 3897.
URL http://www.sciencedirect.com/science/article/pii/S0020768313003041
Saxena, P., Pelteret, J.-P., Steinmann, P., 2015. Modelling of iron-filled magneto-active polymers with a dispersed chain-like microstructure. European Journal of Mechanics - A/Solids 50, 132 – 151.
URL http://www.sciencedirect.com/science/article/pii/S0997753814001508
Schümann, M., Borin, D., Huang, S., Auernhammer, G., Müller, R., Odenbach, S., 2017. A characterisation of the magnetically induced movement of ndfeb-particles in magnetorheological elastomers. Smart Materials and Structures 26 (9), 095018.
URL https://doi.org/10.1088/1361-665x/aa788a
Segurado, J., Llorca, J., 2002. A numerical approximation to the elastic properties of sphere-reinforced composites. Journal of the Mechanics and Physics of Solids 50 (10), 2107–2121.
URL https://doi.org/10.1016/s0022-5096(02)00021-2
Semisalova, A. S., Perov, N. S., Stepanov, G. V., Kramarenko, E. Y., Khokhlov, A. R., 2013. Strong magnetodielectric effects in magnetorheological elastomers. Soft Matter 9 (47), 11318.
URL https://doi.org/10.1039/c3sm52523f
Shiga, T., Okada, A., Kurauchi, T., 1995. Magnetroviscoelastic behavior of composite gels. Journal of Applied Polymer Science 58 (4), 787–792.
URL https://onlinelibrary.wiley.com/doi/abs/10.1002/app.1995.070580411
Spieler, C., Kästner, M., Goldmann, J., Brummund, J., Ulbricht, V., 2013. Xfem modeling and homogenization of magnetoactive composites. Acta Mechanica 224 (11), 2453–2469.
URL http://dx.doi.org/10.1007/s00707-013-0948-5
Spieler, C., Metsch, P., Kästner, M., Ulbricht, V., 2014. Microscale modeling of magnetoactive composites undergoing large deformations. Technische Mechanik 34 (1), 39–50.
Tarantino, M., Zerhouni, O., Danas, K., 2019. Random 3D-printed isotropic composites with high volume fraction of pore-like polydisperse inclusions and near-optimal elastic stiffness. Acta Materialia 175, 331–340.
URL https://doi.org/10.1016/j.actamat.2019.06.020
Zerhouni, O., Tarantino, M., Danas, K., 2019. Numerically-aided 3D printed random isotropic porous materials approaching the hashin-shtrikman bounds. Composites Part B: Engineering 156, 344–354.
URL https://doi.org/10.1016/j.compositesb.2018.08.032
Zhao, R., Kim, Y., Chester, S. A., Sharma, P., Zhao, X., 2019. Mechanics of hard-magnetic soft materials. Journal of the Mechanics and Physics of Solids 124, 244 – 263.
URL http://www.sciencedirect.com/science/article/pii/S0022509618307646
Zurlo, G., Destrade, M., Lu, T., 2018. Fine tuning the electro-mechanical response of dielectric elastomers. Applied Physics Letters 113 (16), 162902.
URL https://doi.org/10.1063/1.5053643